

Relationships between ionospheric parameters derived from ionosonde observations and characteristics of post-sunset GHz scintillation during high solar activities (2012–2013) at Sanya (18.3°N, 109.6°E), China

JunJie Luo¹, Ying Xiong¹, WeiHua Luo^{1,2*}, ZhengPing Zhu^{1,2,3}, and ChaoWan Fan¹

¹College of Electronic and Information Engineering, South-Central Minzu University, 430074 Wuhan, China;

²Hubei Key Laboratory of Intelligent Wireless Communications, South-Central Minzu University, 430074 Wuhan, China;

³Hubei Engineering Research Center of Intelligent Internet of Things Technology, South-Central Minzu University, 430074 Wuhan, China

Key Points:

- Scintillation onset time is found to be correlated with development of the Rayleigh–Taylor instability and with local sunset time.
- Equinoctial asymmetry of scintillation occurrence may be related to background electron density and vertical drift near time of local sunset.
- In low latitudes, ionospheric parameters derived from ionosonde data were not well correlated with scintillation strength.

Citation: Luo, J. J., Xiong, Y., Luo, W. H., Zhu, Z. P., and Fan, C. W. (2023). Relationships between ionospheric parameters derived from ionosonde observations and characteristics of post-sunset GHz scintillation during high solar activities (2012–2013) at Sanya (18.3°N, 109.6°E), China. *Earth Planet. Phys.*, 7(3), 389–406. <http://doi.org/10.26464/epp2023038>

Abstract: In this study, we present characteristics of post-sunset GHz scintillation occurrence and their correlations with ionospheric parameters derived from ionosonde observations in high solar activity years (2012–2013) of solar cycle 24 at Sanya (18.3°N, 109.6°E; dip lat.: 12.8°N), China. The analyzed data include the F_2 -layer's critical frequency (f_oF_2), peak height (h_mF_2), and minimum virtual height ($h'F$), as well as the scale height around the F_2 -layer peak (H_m), and virtual height ($h'F_5$) and true height (hF_5) measured at 5 MHz. We have investigated relationships between the equinoctial asymmetry of these scintillations and these ionospheric parameters. In addition, we calculate the growth rates of Rayleigh–Taylor instability on the basis of the ionosonde measurements and theoretical models, respectively. We find that the equinoctial asymmetry of scintillation onset time is associated with the scale length of the vertical electron density gradient (L), which has been shown to affect the growth of Rayleigh–Taylor instability at the bottom of the F-layer. The seasonal variations of f_oF_2 , H_m and scale length of vertical electron density gradient appear to cause the seasonal variations of scintillation occurrence; the equinoctial asymmetry of scintillation occurrence rate over low latitudes appears to be related to background electron density and vertical drifts in the F-layer around time of sunset. Further study is required to explain the observed correlational weakness in low latitudes between scintillation strength, represented by the daily maximum S_4 , and daily maximum values of f_oF_2 , h_mF_2 , $h'F$, H_m , and also the drifts.

Keywords: equatorial ionosphere; scintillation; low latitude; ionosonde; equinoctial asymmetry

1. Introduction

In equatorial and low-latitude regions, when radio waves of known original strength travel through the ionosphere in the presence of plasma irregularities, amplitudes recorded at receivers beyond the irregularities may fluctuate randomly; this phenomenon is referred to as ionospheric scintillation. Severe scintillation can interrupt satellite communication and navigation systems. Generally, the occurrence of low-latitude plasma irregu-

larities, also referred to as Equatorial Spread F (ESF) or equatorial plasma bubbles (EPB), is attributed to Rayleigh–Taylor (R-T) instability at the bottomside of the F-layer. The characteristics of scintillation and ESF under quiet and disturbed conditions in different longitudinal sectors have been widely studied by means of multi-instrument data collection, which have made it possible to model the irregularity/scintillation and perhaps improve scintillation forecasting.

For instance, in recent years, numerous morphological studies on low-latitude scintillation or ESF in different longitudinal sectors (e.g., the China region) have been made using ionosonde and Global Positioning System (GPS) observations (e.g. Li G et al., 2007; Xu T et al., 2010; Li GZ et al., 2011, 2012, 2013; Liu KK et al., 2015; Zhang Y et al., 2015; Meng X et al., 2018; Wang N et al., 2019; Hu

First author: J. J. Luo, 35126813@qq.com

Correspondence to: W. H. Luo, whluo@mail.scuec.edu.cn

Received 03 FEB 2023; Accepted 23 MAR 2023.

Accepted article online 06 MAY 2023.

©2023 by Earth and Planetary Physics.

LH et al., 2020). These studies have identified the following characteristics: (1) the occurrence of post-sunset scintillation/ESF depends on season and longitude, with the maximum occurring in equinoctial months; (2) the occurrence of scintillation increases with increased solar activity; (3) onset time, occurrence rate, and strength of scintillation all display equinoctial asymmetry.

The equinoctial asymmetry of scintillation (differences between the two equinoxes in scintillation onset times, strengths, and frequencies of occurrence) is especially intriguing, and remains an important open issue in space weather research; it may be a key to understanding the factors that control the occurrence of ESF irregularities and scintillation (Maruyama et al., 2009).

Relevant studies focused on certain sectors of longitude during various different periods of solar activity have been reported and discussed. Maruyama et al. (2009) studied the equinoctial asymmetry of ESF during moderate solar activity along the 100°E sector, using ionosonde observations in model calculations. They found that the meridional wind may play an important role in causing the equinoctial asymmetry in occurrence of irregularities, suggesting that transequatorial wind would suppress the initiation of R-T instability and the occurrence of ESF. Sripathi et al. (2011) report an equinoctial asymmetry of L-band scintillation occurrence over the Indian region when solar activity was moderate during solar cycle 23; they attributed that asymmetry to differences in the background electron density. Manju et al. (2012) reported a significant equinoctial asymmetry in ESF occurrence at magnetic equator and low-latitude regions in Indian regions during periods of moderate to low solar activity (2004–2007). They suggested that neutral dynamics may act as one candidate contributing to the equinoctial asymmetry in the occurrence of ESF, higher $[O/N_2]$ was found at the vernal equinox compared to the autumnal equinox (Manju et al., 2015). Sousasantos et al. (2018) reported a seasonal asymmetry of L-band scintillation onset time over the Brazilian region in data from 1998 to 2014, and suggested that the observed asymmetry may be related to time and magnitude of ionospheric prereversal vertical drift. Afolayan et al. (2019) reported a seasonal asymmetry in the range spread F occurrence at five different longitudes at times of low and moderate solar activity.

On the other hand, based on ionosonde measurements, such as variations in virtual height ($h'F$) and critical frequency of the F-layer, some studies on the onset conditions for the post-sunset ESF, such as Abdu et al. (1982), have shown that scale length of electron density gradient and ion-neutral collision frequency at the bottomside of the F layer near local sunset appear to determine the post-sunset onset of ESF. Jayachandran et al. (1993) investigated the relative importance of $h'F$, vertical drift (V_z), and vertical density gradient (dN_e/dh) to the linear growth rate of the R-T instability that precedes the onset of spread F. They computed the linear growth rate of the R-T instability using vertical drift and density gradient data, and found that height and drift velocity are the deciding factors for the onset of ESF, with little contribution from the electron density gradient. Also, Manju et al. (2009) used ionosonde measurements, collected during different seasons and solar cycles in the Indian region, to study variations of electron density gradient scale length (L), vertical drift, and layer height.

Their results showed that scale length, too, plays an important role in controlling seasonal and solar cycle variability of ESF under quiet conditions. Lee CC (2010) analyzed statistically the onset conditions of ESF in the Peruvian sector, using ionospheric parameters derived from ionosonde measurements, and found that the occurrence of ESF was independent of solar cycle, and can be attributed to variations in ion-neutral collision frequency and recombination rate. Recently, Abdu et al. (2020) pointed out that the bottomside density gradient (scale length) appears to be a key parameter controlling the development of equatorial and low-latitude irregularities, based on digisonde observations at times of high and low solar activity.

However, the factors causing the equinoctial asymmetry of scintillation occurrence in equatorial and low-latitude regions remain poorly understood, and little study has been made of ionosonde data to determine whether scintillation or irregularities might appear in those regions at times of high solar activity, and, if so, which factors are likely to account for such appearances. Recently, Hu LH et al. (2020) reported an equinoctial asymmetry in the occurrence rate of plasma plume at Sanya. For instance, in 2011 the occurrence rate of plasma plume was higher in autumn months than in spring months. They attributed this asymmetry to the asymmetric vertical drifts. Meanwhile, ionosonde observations over southern China have been used to characterize ionospheric parameters (e.g. Wang N et al., 2018), but these parameters have not been related to characteristics of scintillation.

In this study, we have attempted to investigate statistical relationships between ionospheric parameters and occurrences of scintillation and/or irregularities. Our work is based on ionosonde observations during periods of high solar activity (2012–2013) in solar cycle 24 at Sanya (18.3°N, 109.6°E; dip lat.: 12.8°N), China, including data related to F_2 -layer critical frequency (f_oF_2), peak height (h_mF_2), and minimum virtual height ($h'F$), as well as scale height around the F_2 -layer peak (H_m), which is a measure of the electron density profile slope of the topside ionosphere (e.g. Liu L et al., 2006), and virtual height at 5 MHz ($h'F_5$) and true height (hF_5) measured at 5 MHz (e.g. Li GZ et al., 2013; Abdu et al., 2020). Furthermore, we then discuss the relationships found between scintillation strength and the ionospheric parameters.

2. Data

The GHz scintillation data were recorded by the GPS Ionospheric Scintillation and TEC Monitor (GISTM) system GSV4004A at Sanya, which calculated the amplitude index (S4) in time intervals of 1 min (e.g. Li GZ et al., 2008, 2012). To eliminate multi-path effects, the S4 data with elevation angles larger than 30° and lock time more than 3 minutes were used. The threshold 0.2 of S4 was used to identify occurrences of scintillation (Liu KK et al., 2015); “strong” scintillation was defined as S4 of at least 0.5.

The ionospheric parameters data, including of the various F_2 -layer characteristics mentioned above (Titheridge, 1988), were derived manually from the Digisonde Portable Sounder (DPS-4D) observations every 15 minutes at Sanya. There were no available ionosonde records during 3–7 December in 2012, and 11–25 November in 2013, which would not affect the focuses of this study. It should be noted that the estimation of virtual height may


have an uncertainty under normal conditions of no disturbances (Jayachandran et al., 1993). For more details of the uncertainties associated with the derived results, see the work by Balan et al. (1992).

Vertical drifts of the F-layer were calculated as proposed by Bittencourt and Abdu (1981). Some studies have indicated that, in equatorial and low-latitude regions, the drifts derived from $h_m F_2$ are similar to those from $h'F$ (e.g. Yue et al., 2008; Adebesein et al., 2015). In this study, the time rates of $h'F_5$ and hF_5 were calculated to represent the movement of the F layer, and described as the $E \times B$ drift.

$$V_{h'F_5} = \frac{dh'F_5}{dt},$$

$$V_{hF_5} = \frac{dhF_5}{dt}.$$

It should be noted that the variations of height would include the effects from both the zonal electric field and meridional neutral wind in low-latitude regions (e.g. Abdu et al., 2006), which play an important role in the development of R-T instability and the occurrence of ESF/scintillation.

In Figure 1, for example, we present the variations of ionospheric parameters inferred from ionosonde measurements around sunset during 10:00–12:00 Universal Time (UT), and also variations of the S4 index after sunset on scintillation days during Spring (a) and Fall (b) equinoxes in 2012, respectively. The symbol  represents the local sunset time. The average sunset time was 11:25 UT (Local Time (LT) = UT+7.5) during the Spring equinox and 11:00 UT during the Fall equinox in 2012 and 2013, respectively.

In Figure 1, it can be seen that the relationships between ionospheric parameters and scintillation on scintillation days differed between the two equinoctial months. For instance, the vertical drifts around local sunset were remarkable larger during Spring than during Fall. The onset of scintillation during Spring (e.g. DOY101) was later than onset during the Fall equinox.

The profiles of electron density (N_e) with altitude were obtained from the ionograms by the Automatic Real-Time Ionogram Scaler with True height (ARTIST) (Galkin et al., 2008). The scale length (L) of vertical density gradient is calculated as

$$\frac{1}{L} = \frac{1}{N_e} \frac{\partial N_e}{\partial h}.$$

3. Observations and Results

3.1 Characteristics of GHz Scintillation

Total observations (TO) is defined as the sum of all observations in which the elevation angles of the S4 data were larger than 30° and the lock time exceeded 3 minutes. Scintillation occurrences (SO) include all observations in which the values of S4 were larger than the chosen threshold. Excluded from both are any data collected under disturbed conditions. The scintillation occurrence rate (P) was calculated as below,

$$P = \frac{SO}{TO} \times 100\%.$$

Figure 2 displays monthly variations in the post-sunset GHz scin-

tillation occurrence rate (top panel), the occurrence rate of strong scintillation (middle panel), and also the $F_{10.7}$ index (bottom panel) during high solar activity in 2012 (a) and 2013 (b), respectively. As shown in Figure 2, the monthly average $F_{10.7}$ indices during the two equinoxes were comparable to those in other months of 2012 and 2013. Solar activity during September 2013 was relatively lower than in 2012. Total scintillation occurrences as well as strong scintillation occurrences were remarkably higher in both Spring (March–April) and Fall (September–October) equinox months than in other months, and the occurrences were lowest during the two solstices, results which are consistent with previous studies (e.g. Liu KK et al., 2015).

The equinoctial asymmetry was observed. In 2012, the highest scintillation occurrence was in September; in 2013 the highest rate occurred during April. The equinoctial asymmetry of scintillation occurrence was more remarkable in 2013 than in 2012. In 2012, the scintillation occurrence rates were comparable between the two equinoxes, though the occurrence rates were slightly larger in September. In 2013, the scintillation occurrence was significantly higher in April than during the Fall equinox. The solar activity in October was high, the scintillation occurrence rate was less than that in other equinoctial months, which means that the seasonal asymmetry of scintillation occurrence may be not associated with solar activity.

Figure 3 displays the distributions of post-sunset S4 index ($S4 > 0.2$) during the equinoxes in 2012–2013. In 2012 and 2013, the onset of scintillation occurred earlier in the Fall equinox period than in that of the Spring equinox; a 40-minute average onset-time difference was noted between the two equinoxes.

Figure 4 displays the day-to-day variations of daily maximum S4 index ($S4_{max}$), and the monthly mean $S4_{max}$ in 2012 and 2013. In the figure, only $S4_{max}$ values larger than 0.2 are presented. Note that the scintillation strengths displayed in Figure 4 clearly show the seasonal variations in 2012–2013. The monthly averages of $S4_{max}$ (larger than 0.5) during the two equinoctial months were larger than those in other seasons. In addition, the scintillation strength also displays asymmetry. Similar to the scintillation occurrence rate, shown in Figure 2, the equinoctial strength asymmetry was more significant in 2013 than that in 2012. In 2012, the monthly $S4_{max}$ averages were comparable in equinoctial months; in 2013, however, the monthly $S4_{max}$ averages during March–April were larger than during September–October.

3.2 Characteristics of Ionospheric Parameters from Ionosonde Measurements

3.2.1 Variations of ionospheric parameters around local sunset

Figure 5 presents variations of ionospheric parameters observed from 10:30 to 12:00 UT, local sunset time, in 2012 (a) and 2013 (b), respectively. The parameters in question are f_oF_2 , $h_m F_2$, minimum $h'F$, and H_m . It should be noted that these ionospheric parameters cannot be determined to any degree of accuracy under spread F conditions (Jayachandran et al., 1993); for that reason, the data presented in Figure 5 are limited to those collected before scintillation onset.

As shown in Figure 5, at different UT times (around sunset), in

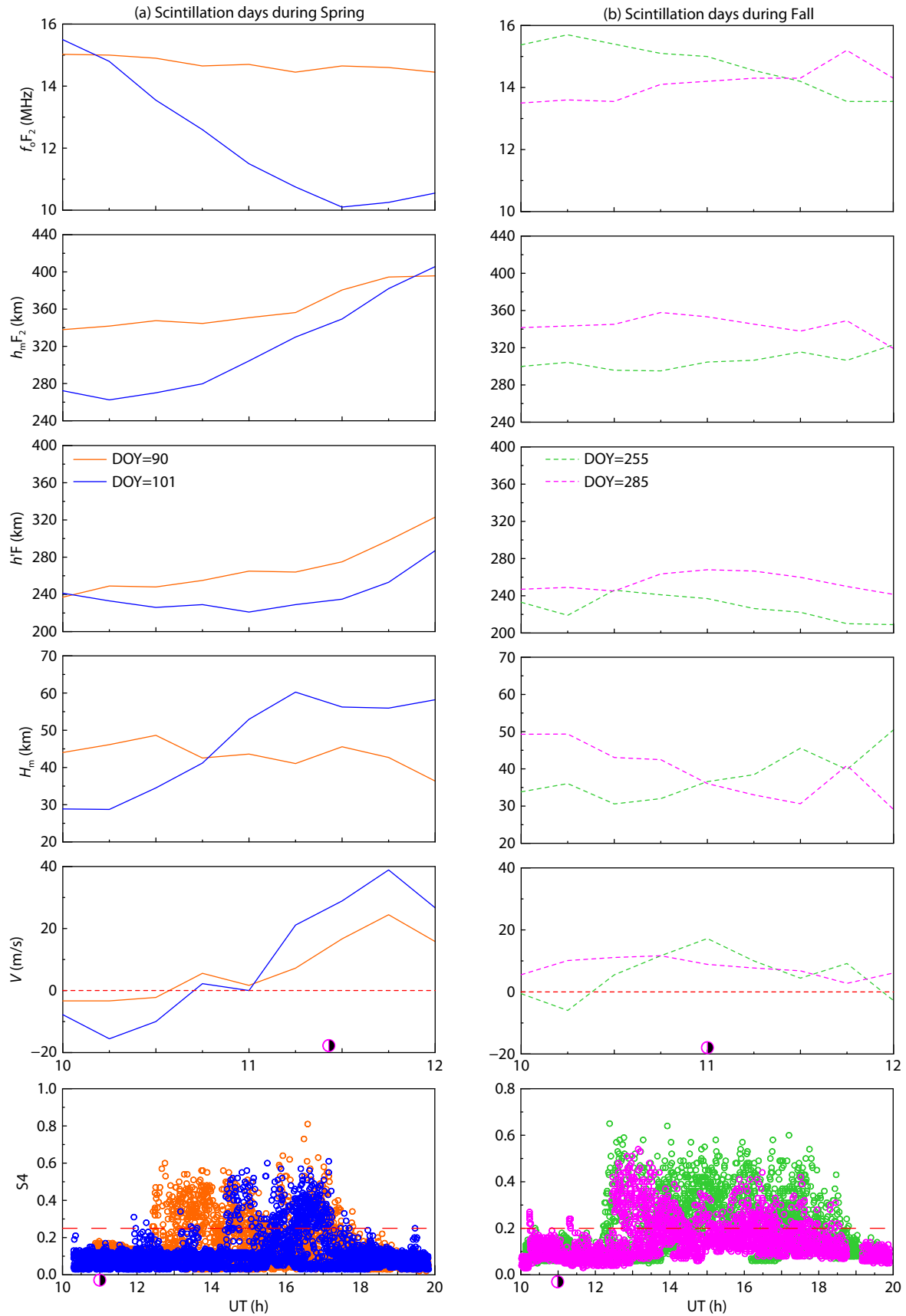



Figure 1. An example of variations of ionospheric parameters (f_oF_2 , h_mF_2 , $h'F$, H_m and vertical drift) around local sunset inferred from ionosonde measurements, and also the variations of post-sunset S4 index on scintillation days during Spring (a) and Fall (b) equinoxes, respectively, in 2012. The red dashed lines in the bottom panel represent the S4 threshold value ($S4 = 0.2$). The symbol  represents the sunset time.

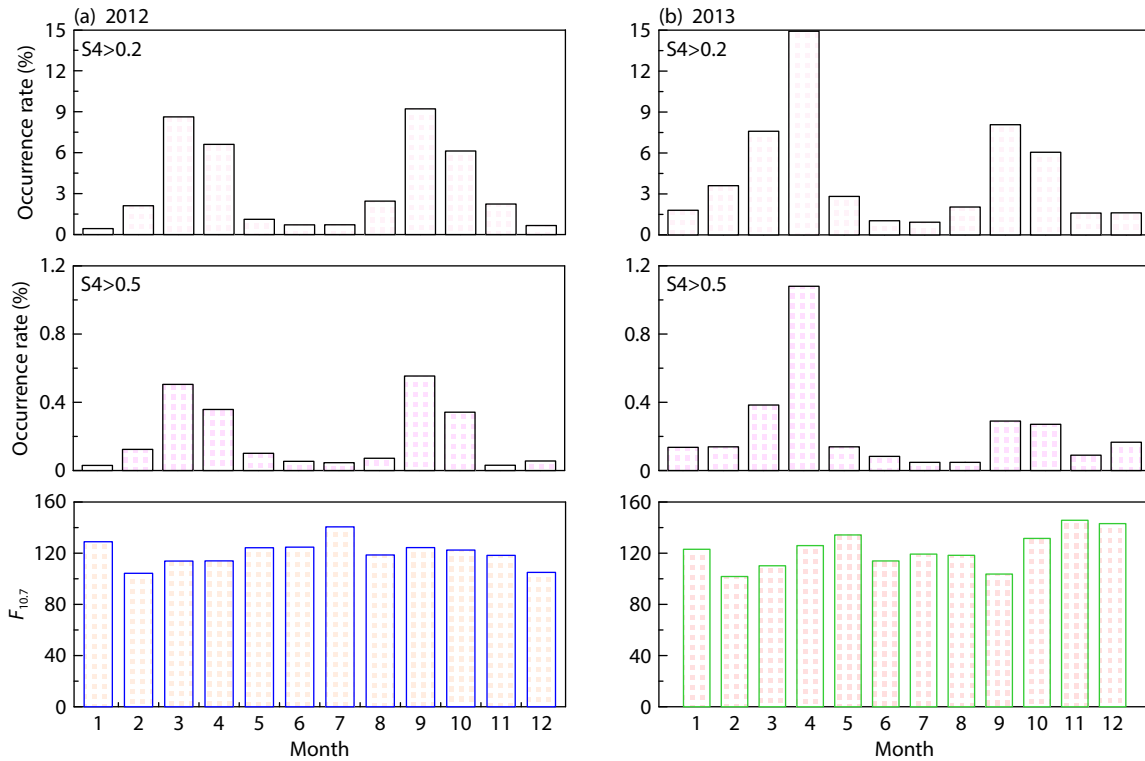


Figure 2. Monthly variations of post-sunset scintillation occurrence rate ($S4 > 0.2$, top panel), strong scintillation occurrence rate ($S4 > 0.5$, middle panel), and $F_{10.7}$ indices (bottom panel) under quiet conditions during high solar activity in 2012 (a) and 2013 (b).

high solar activity, the monthly mean f_oF_2 reached its maximum in equinoctial months, while monthly mean H_m reached its minimum. The monthly mean h_mF_2 and mean $h'F$ reached their peaks in equinoctial months, similar to f_oF_2 . At 12:00 UT, after local sunset, the parameters clearly showed the expected equinoctial asymmetry, especially in 2013. Generally, the monthly averages of f_oF_2 , h_mF_2 , and $h'F$ during the Spring equinox were larger than during the Fall equinox, while the monthly mean H_m exhibited the opposite pattern — smaller at Spring equinox than at Fall equinox.

Figure 6 shows day-to-day variations of drifts, derived from $h'F_5$ data around sunset in equinoctial months at 11:00 UT (top), 11:30 UT (middle) and 12:00 UT (bottom) in 2012 (a) and 2013 (b), respectively. The equinoctial months are marked by the shaded blocks; the short red lines represent the monthly mean values. At 11:00 UT, in 2012 and 2013, the drifts ($dh'F_5/dt$) showed the evident equinoctial asymmetry, values at Fall equinox season being larger at Spring equinox. At 11:30 UT, in 2012 and 2013, the drifts decreased obviously in October; however, during the Spring and Fall equinox periods they were close in magnitude, exhibiting no obvious asymmetry. At 12:00 UT, the drifts in April were larger than in other equinoctial months. The average drifts in March and in October turned downward; the drift decreased in September. In 2012 and 2013, the average drifts in October reached their maximum around 11:00 UT (near sunset); it was at 11:30 UT (also near sunset) that maximum average drifts were observed in March–April.

In Figure 7, we display variations around sunset — at 11:00 UT, 11:30 UT and 12:00 UT in 2012 and 2013, respectively — of monthly L^{-1} average (a) and the temporal gradient of monthly

mean L^{-1} (b). Figure 7 shows that monthly mean L^{-1} displayed evident equinoctial asymmetry at 11:00 UT and 11:30 UT, the asymmetry decreasing at 12:00 UT. In 2012 and 2013, the monthly mean L^{-1} was larger at 11:00 UT and 11:30 UT during the Fall equinox than during the Spring equinox; during the Spring equinox, the mean L^{-1} became larger at 12:00 UT. From Figure 7b, we can notice that the temporal rates of monthly mean L^{-1} at 11:00 UT during the Fall equinox months were more pronounced than during the Spring equinox. But at 11:30 UT and 12:00 UT, the temporal gradients of monthly mean L^{-1} were larger during the Spring equinox, which means that the variations of L^{-1} with time were more remarkable.

3.2.2 Comparisons between the two equinoxes around sunset

As Sridharan et al. (2014) and Bagiya et al. (2014) indicated, occurrences of L-band scintillation in low-latitude regions may be related to the variations of total electron content (TEC) during the hours of 17:30–19:30 LT. The day-to-day variations and seasonal averages of f_oF_2 and H_m during the two equinoxes around local sunset in 2012 (a) and 2013 (b), respectively, are shown in Figure 8. In 2012, the monthly f_oF_2 means during both equinoxes were comparable at local sunset time — though larger around sunset and smaller after sunset in the Fall equinoctial period, compared to the Spring. The monthly mean H_m around sunset during the Fall equinox was smaller than during Spring equinox. The scintillation occurrence rates were also comparable between the two equinoxes, though the occurrence rate in the Fall equinox was slightly higher. In 2013, the monthly mean f_oF_2 around sunset during the Spring equinox was obviously larger than during the Fall equinox. The scintillation occurrence rate, too, was higher

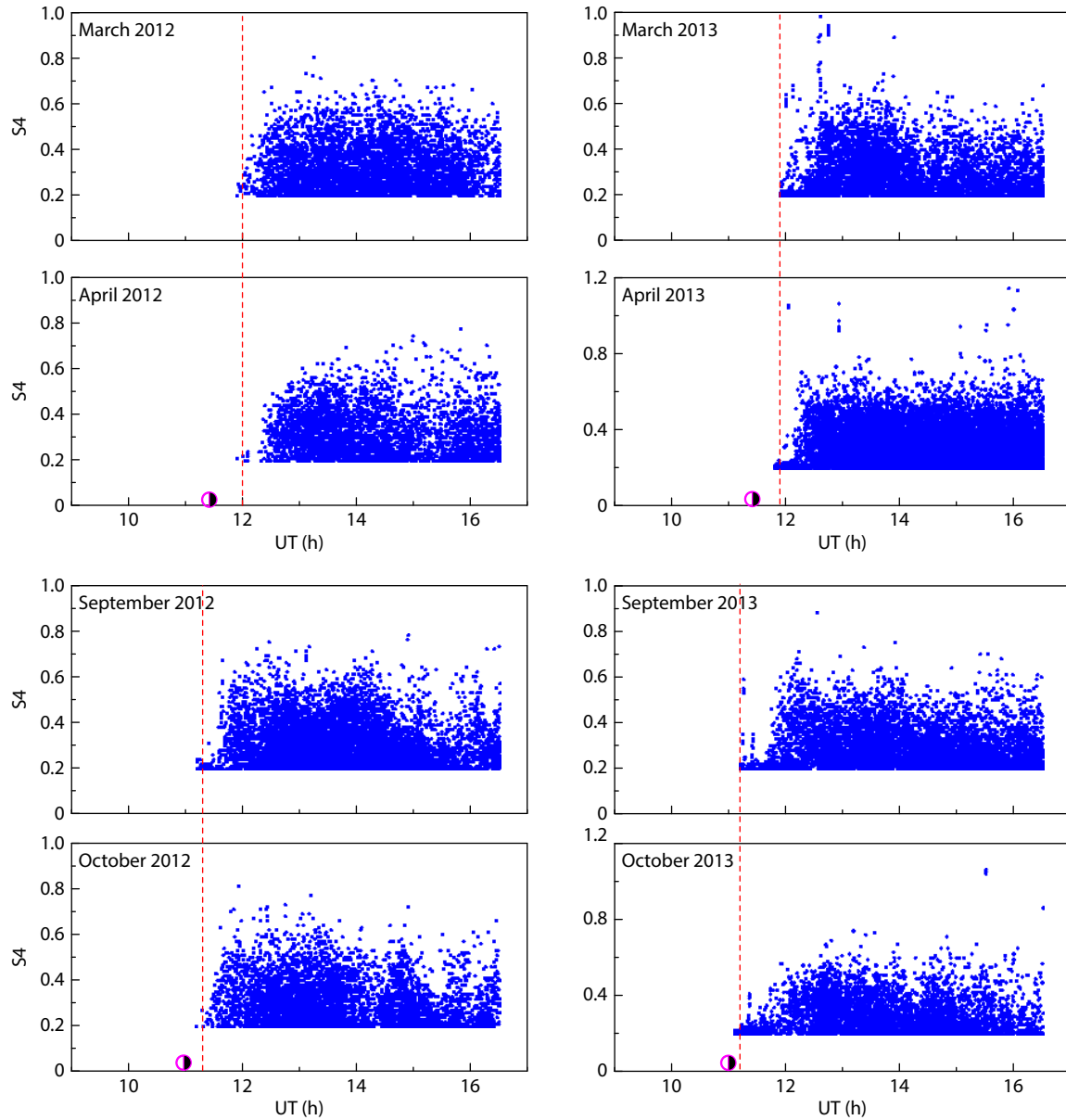
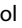


Figure 3. Distributions of post-sunset S4 index ($S4 > 0.2$) during the equinoctial months in 2012 (left panel) and 2013 (right panel). The red dashed lines represent the average onset time of GHz scintillation. The symbol  represents the sunset time.

during Spring than during Fall. However, the equinoctial monthly H_m means at sunset exhibited the opposite asymmetry — smaller in Spring than in Fall. In 2012 only small differences were recorded between the equinoctial monthly means of f_oF_2 and H_m , and the Spring and Fall scintillation occurrence rates, too, were closer than in 2013. Thus monthly equinoctial f_oF_2 and H_m means appear to correlate with scintillation occurrence rates.

Figure 9 shows the day-to-day variations of drifts derived from the $h'F_5$ around sunset during the equinoxes in 2012 (a) and 2013 (b), respectively. The red bars represent the monthly average of $(dh'F_5/dt)$ in March, September, April, and October, respectively. At local sunset time (middle panel of Figure 9), in 2012 and 2013, the average drifts in March were larger than in September, while the average drifts in October were larger than in April. After sunset (bottom panel of Figure 9), in 2012 and 2013, the average

drifts in March–April were larger than in September–October.

Figure 10 presents the day-to-day variations of L^{-1} around local sunset in equinoctial months in 2012 and 2013, respectively. From Figure 10, we can see that the L^{-1} around local sunset displays evident asymmetry between the two equinoxes. Generally, the smaller the L^{-1} value, the higher the scintillation occurrence rate. In 2013, the monthly mean L^{-1} was larger in September–October than in March–April, when the scintillation occurrence rate was higher. In 2012, the differences of L^{-1} between the two equinoxes were small near sunset, but after sunset a difference did become obvious: the average L^{-1} was smaller and the scintillation occurrence rate was higher in the Fall equinoctial period.

3.3 Linear Growth Rate of R-T Instability

The linear growth rate of R-T instability, which describes the linear

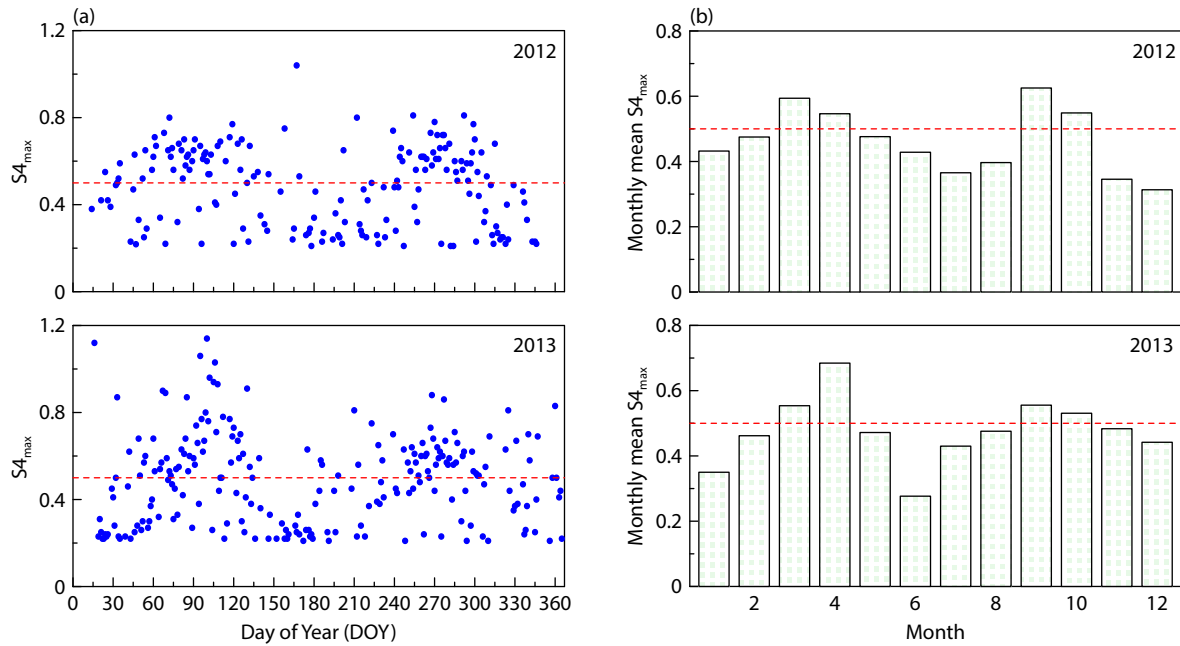


Figure 4. Day-to-day variations of the daily S4 maximum (a), and the monthly average of daily S4 maximum (b) in 2012 (top panel) and 2013 (bottom panel). The red dashed lines represent $S4 = 0.5$.

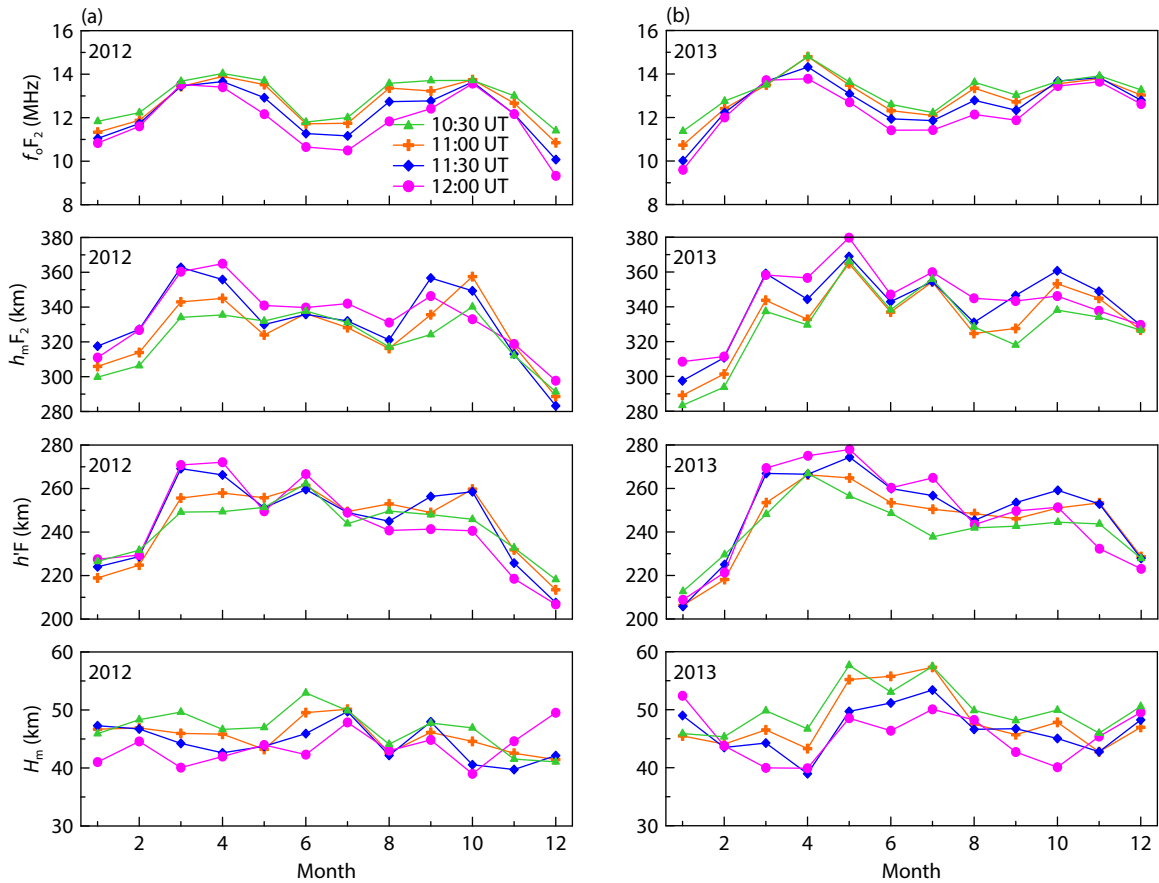


Figure 5. Variations of monthly mean f_oF_2 , h_mF_2 , minimum $h'F$, and H_m at different UT times (around local sunset) in 2012 (a) and 2013 (b). The green, orange, blue and magenta lines represent the monthly mean parameters at 10:30 UT (green), 11:00 UT (orange), 11:30 UT (blue) and 12:00 UT (magenta).

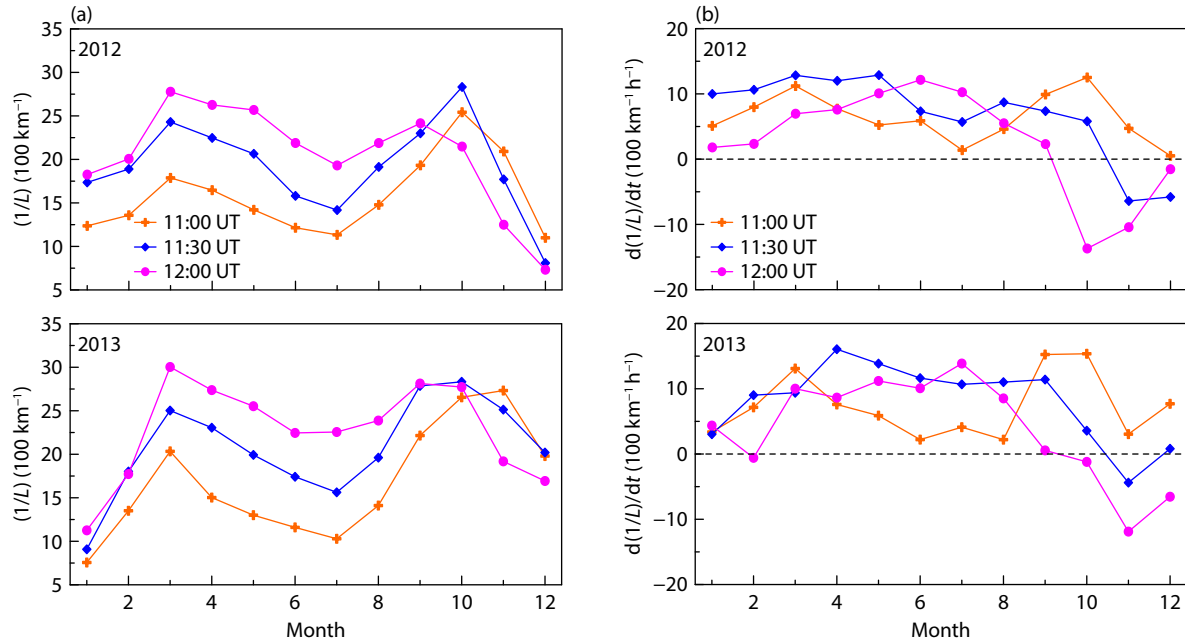


Figure 6. Day-to-day variations of drifts ($dh'F_5/dt$) at 11:00 UT (top), 11:30 UT (middle), and 12:00 UT (bottom) in 2012 (a) and 2013 (b). The red short lines in the blocks represent the monthly average of ($dh'F_5/dt$).

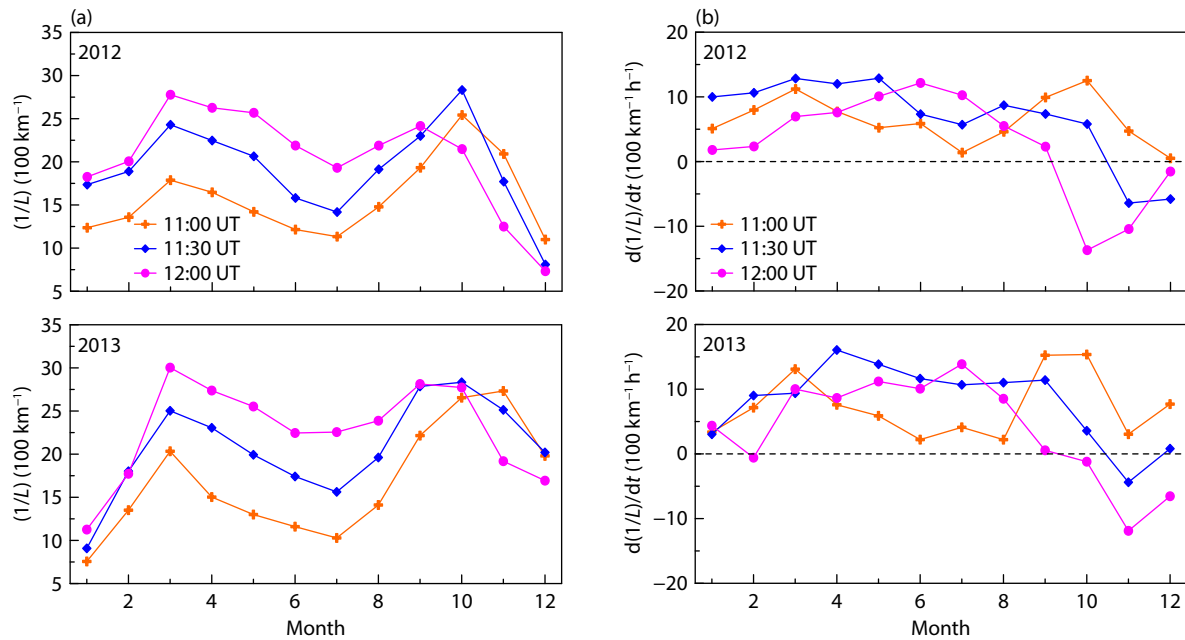


Figure 7. Variations of monthly mean L^{-1} (a) and the temporal gradient of monthly mean L^{-1} (b) at 11:00 UT (orange), 11:30 UT (blue) and 12:00 UT (magenta) in 2012 and 2013.

stage of the R-T instability and can be used to predict the expectation of plasma irregularities in the equatorial ionosphere (Basu, 2002), has been used to study the occurrence and characteristics of ESF (e.g. Luo WH et al., 2012, 2013; Wu Q, 2015, 2017; Shinagawa et al., 2018). In the theory of R-T instability, the ballooning-mode type (three-dimensional) description is the most accurate to describe the linear development of R-T instability and equatorial plasma irregularities (Basu, 2002). In dipole coordinate system (q , s ,

λ), the three-dimensional linear growth rate (γ) of R-T instability can be described as (e.g. Basu, 2002; Luo WH et al., 2013)

$$\gamma = \frac{1}{\eta_0 L_{nq}} \left(\frac{g}{v_{in}} + \frac{E_s}{B} - U_q + \frac{v_{in} E_q}{\Omega_i B} + \frac{v_{in} U_s}{\Omega_i} \right) - \beta, \quad (1)$$

$$\eta_0^{-1} = \frac{\sigma_p / \sigma_{||}}{\sigma_p / \sigma_{||} + k_t^2 / k_s^2}$$

where L_{nq} represents the scale length of the vertical density gradi-

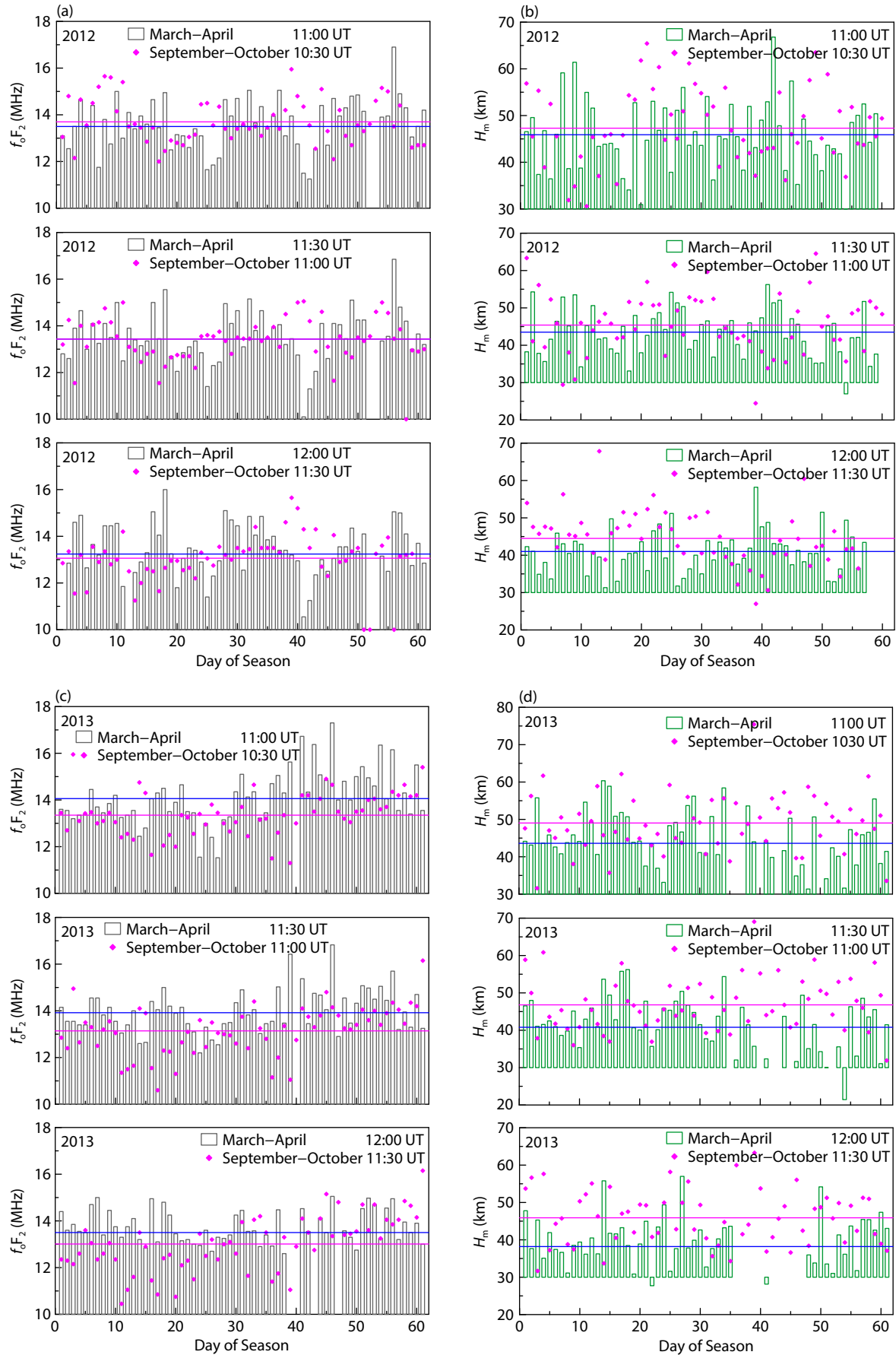


Figure 8. Day-to-day variations of f_oF_2 (a and c) and H_m (b and d) during two equinoxes before local sunset (top), at sunset (middle), after sunset (bottom) in 2012 and 2013. The blue and magenta lines represent the mean values in March–April and September–October, respectively.

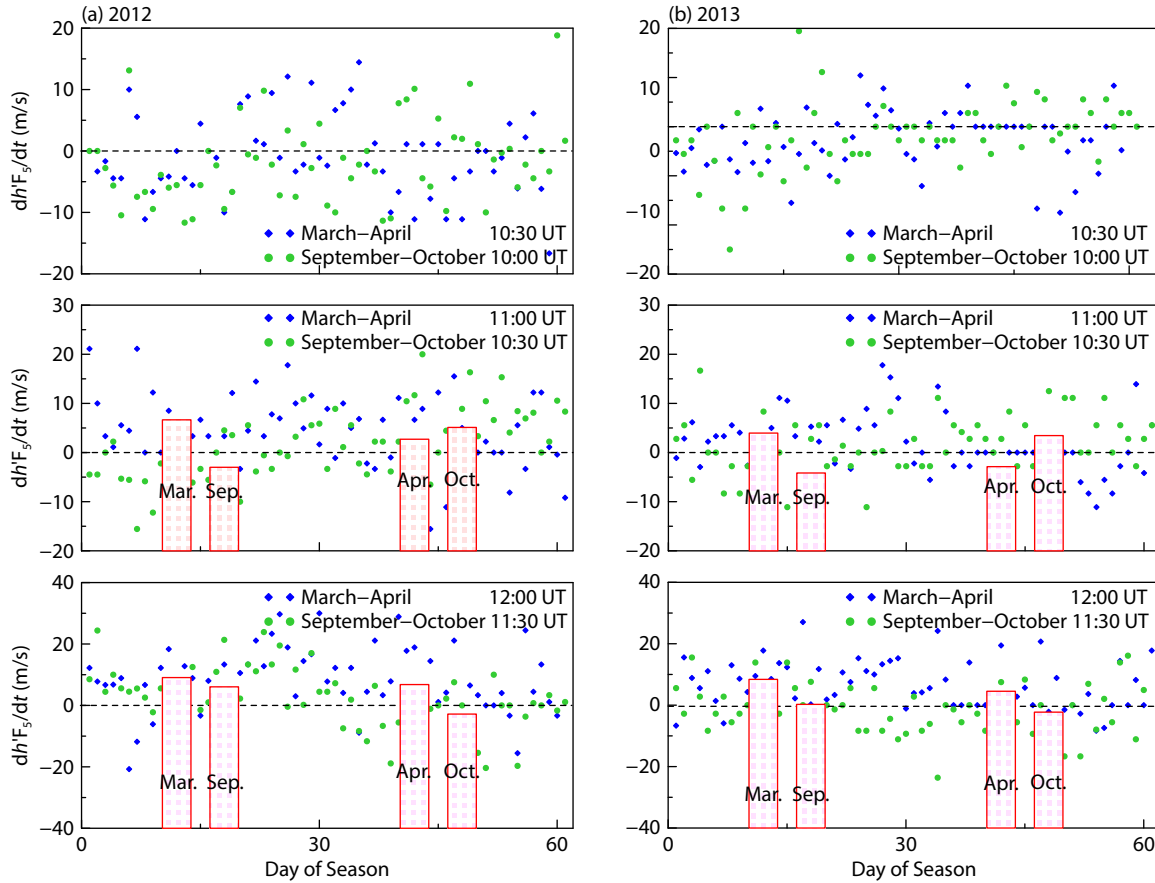


Figure 9. Day-to-day variations of drifts ($dh'F_5/dt$) before local sunset (top panel), at sunset (middle panel) and after sunset (bottom panel) during the equinoctial months in 2012 (a) and 2013 (b). The red bars represent the monthly average of ($dh'F_5/dt$) in March, September, April, and October.

ent, ν_{in} is the ion-neutral collision frequency, \mathbf{B} is the magnetic field, Ω_i is the gyrofrequency of ions, E_s and E_q represent the background zonal and vertical electric field, and U_q and U_s represent, respectively, the vertical and zonal winds. β is the recombination rate. η_0 is the coefficient about the wave number in zonal (k_s) and parallel (k_{\parallel}) directions, Pedersen conductivity (σ_p) and parallel conductivity (σ_{\parallel}); see Luo WH et al. (2013) and Basu (2002) for details.

For simplicity, the local R-T instability growth rate derived from ionosonde observations was calculated as

$$\gamma_I = \frac{1}{N_e} \frac{\partial N_e}{\partial h} V_{h'F_5} = \frac{1}{L} V_{h'F_5}, \quad (2)$$

where the subscript I signifies that the growth rate is derived from ionosonde observations.

In Equation (2), the effects of collision, neutral wind, and recombination are neglected, leading to differences compared to results from Equation (1), but this simplified equation nevertheless represents the development of R-T instability with reasonable accuracy (e.g. Abdu et al., 1982; Jayachandran et al., 1993).

To calculate the linear growth rate in Equation (1), we used ionospheric and atmospheric models, including International Reference Ionosphere (IRI)-2016 (Bilitza et al., 2017), and Horizontal Wind

Model (HWM)14 (Drob et al., 2015), NRL-MSIS00 (Picone et al., 2002). Our vertical $\mathbf{E} \times \mathbf{B}$ drift related to the zonal electric field was calculated using the empirical drift model derived from ROCSAT-1 (Fejer et al., 2008); in the calculation, we have used the solar flux ($F_{10.7}$), ap index; the altitude was chosen as 250 km.

3.3.1 Growth rate from the observations

Figure 11 presents the day-to-day variations of growth-rate (γ_I) calculated by applying Equation (2) to ionosonde observations at 250 km collected around local sunset during the equinoctial months in 2012 (a) and in 2013 (b), respectively. The monthly averages of γ_I in March, September, April, and October are marked as green bars. Figure 11 reveals, in both years, a significant asymmetry between monthly average of growth rates observed during each year's two equinoxes. Around sunset, in general, the growth rates during the Fall equinox were larger than during the same year's Spring equinox. The average growth rates in March and September were comparable, but the growth rate in October was remarkably larger than in April. The larger growth rates during the Fall equinox imply that the R-T instability developed faster in September–October than that in March–April.

3.3.2 Growth rate from the models

Figure 12 displays the R-T instability growth rates calculated from

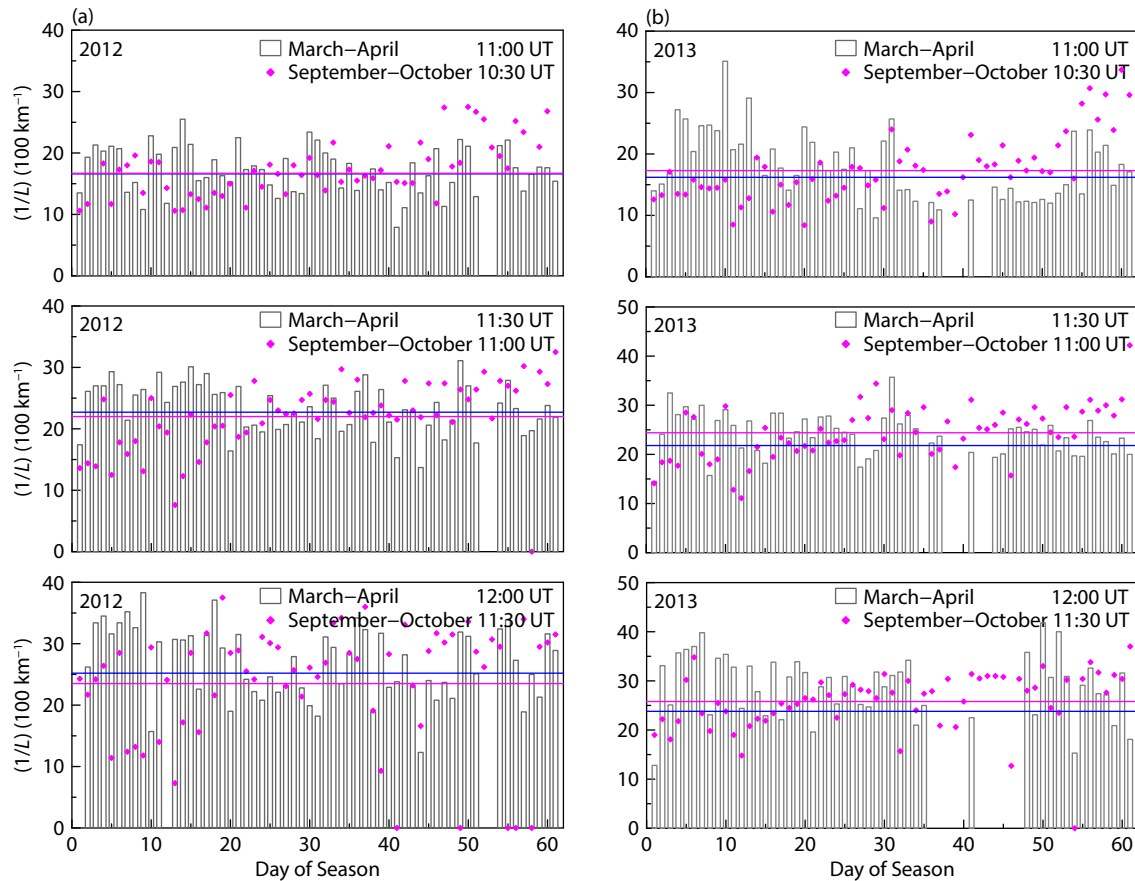


Figure 10. Day-to-day variations of L^{-1} before local sunset (top panel), at sunset (middle panel) and after sunset (bottom panel) in equinoctial months in 2012 and 2013. The blue and magenta lines represent the mean values in March–April and September–October, respectively.

Equation (1) based on the models for the equinoctial months in 2012 and 2013, respectively. Also presented is the correlation between the growth rates derived from ionosonde data (vertical axis) and the growth rates from the models (horizontal axis).

The remarkable equinoctial asymmetry is clearly presented in the modeled growth rates for both years, and, as seen in the observed data (Figure 11), the modeled growth rates in September–October are clearly larger than in March–April.

Although the overall patterns of the growth rates thus agree, the actual growth rate magnitudes derived from ionosonde observations are not well correlated with the growth rates from the models, with moderate coefficients. The differences between growth rates based on the ionosonde observations and the growth rates from the models can be attributed to the fact that the modeled growth rates include the effects of neutral wind, collision, and also recombination.

3.4 Relationship Between the Scintillation Strength and Ionospheric Parameters

Many studies have suggested that monitoring the vertical drift, $h'F$, and $h_m F_2$ may allow prediction of the occurrence of post-sunset irregularities (e.g. Anderson et al., 2004; Devasia et al., 2002; Huang CS, 2018). Moreover, Whalen (2009) indicated that the maximum S4 may be linearly associated with the maximum electron density of F_2 -layer ($N_m F_2$). Li GZ et al. (2021) also

mentioned that the irregularity and resultant scintillation strengths are likely to be related to the background ionospheric density.

To investigate possible relationships between the scintillation strength and the ionospheric parameters, we display in Figure 13 the correlations between the daily maximum S4 ($S4_{max}$) and the following parameters: the daily maximum $f_o F_2$ (a), the $h_m F_2$ (b), the minimum $h'F$ (c), the H_m (d), and also the drifts dhF_5/dt (e) and $dh'F_5/dt$ (f), all derived from ionosonde measurements made in 2012 and 2013, respectively, during the two equinoxes each year. It can be seen in Figure 13 that the correlations between daily scintillation strength and daily parameter extremes were poor when solar activity was high. It is also clear that, similarly, the daily maximum S4 was not well correlated with the dhF_5/dt or $dh'F_5/dt$ at times of high solar activity. Dabas et al. (2007) reported that, in the equatorial region of the Indian sector, post-sunset 4 GHz scintillation intensity was not well correlated with the $E \times B$ drift during evening hours. These observations imply that the relationships between scintillation strength and ionospheric parameters inferred from multiple measurements need further study.

4. Discussion

As presented in Figures 2–4, equinoctial scintillation in low-latitude regions exhibit annual asymmetries in occurrence rate, onset time, and strength, that are not obviously linked to annual sunspot number. Scintillation in the low-latitude regions is instead associ-

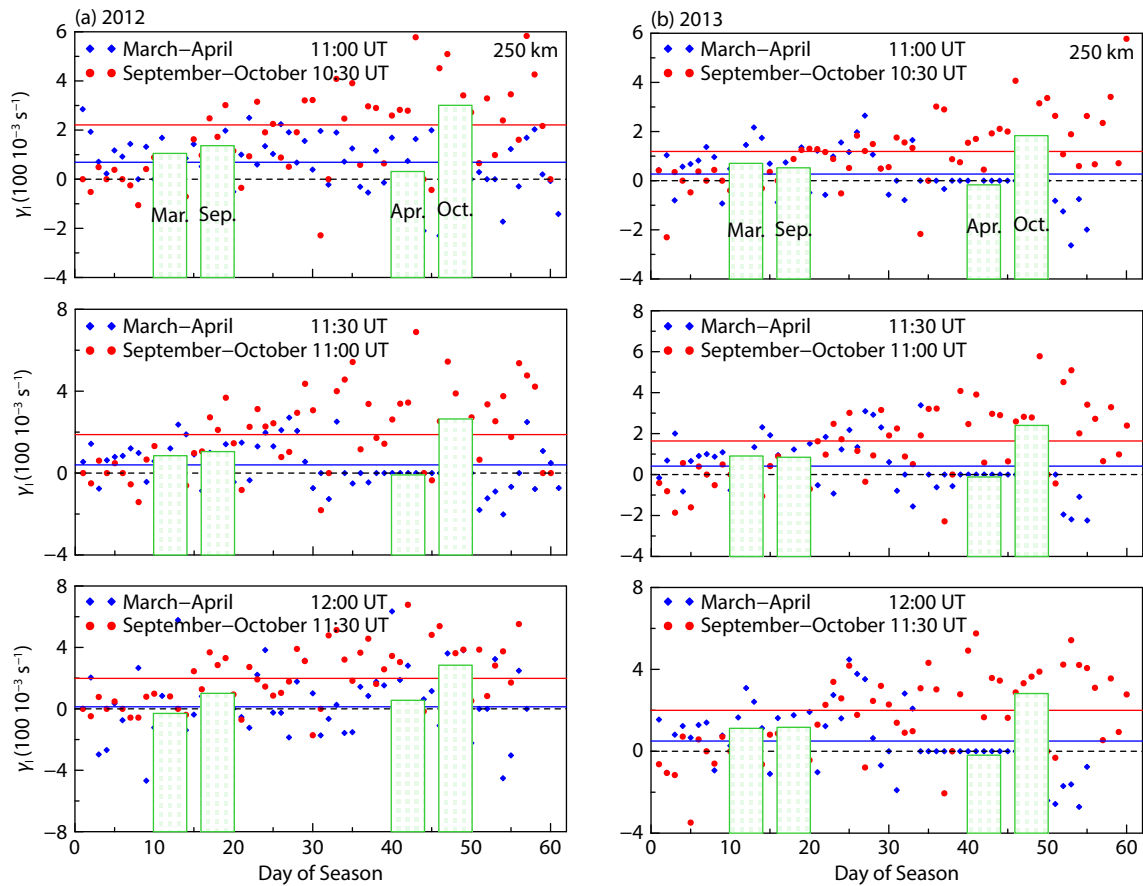


Figure 11. Day-to-day variations of the growth rate from ionosonde measurements before local sunset (top panel), at sunset (middle panel) and after sunset (bottom panel) during equinoctial months in 2012 (a) and 2013 (b). The blue and red lines represent the mean values in March–April and September–October, respectively. The green bars represent the monthly mean values in March, September, April, and October.

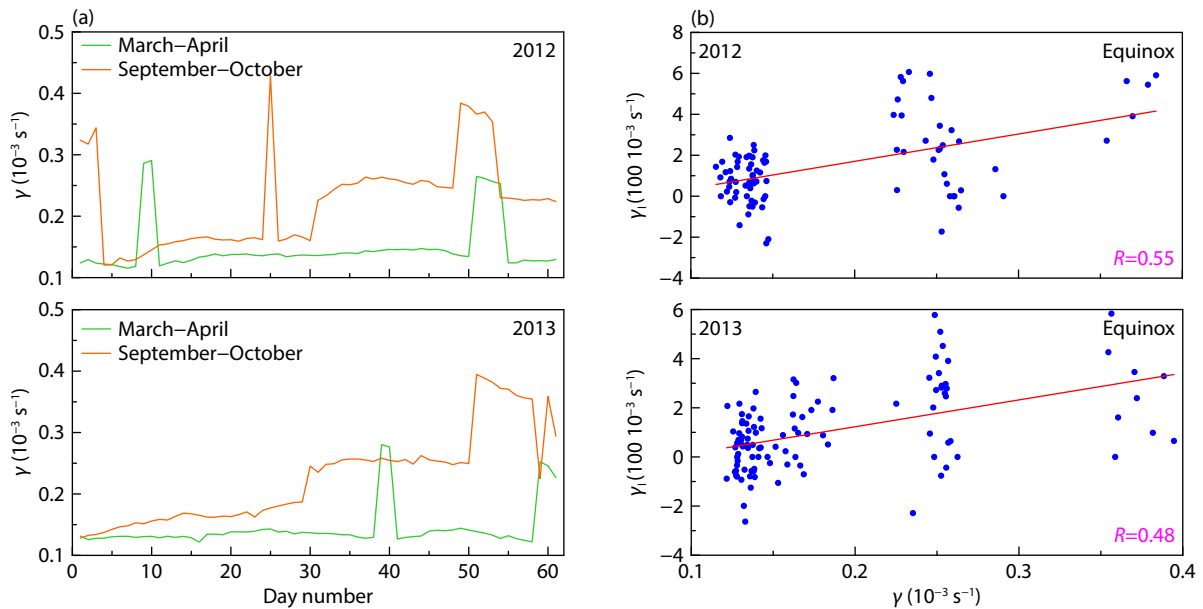


Figure 12. Day-to-day variations of the growth rate of R-T instability from the models during two equinoxes in 2012 and 2013 (a), and the correlation between the growth rate from ionosonde observations (vertical axis) and the growth rate from the models (horizontal axis) during two equinoxes in 2012 and 2013 (b).

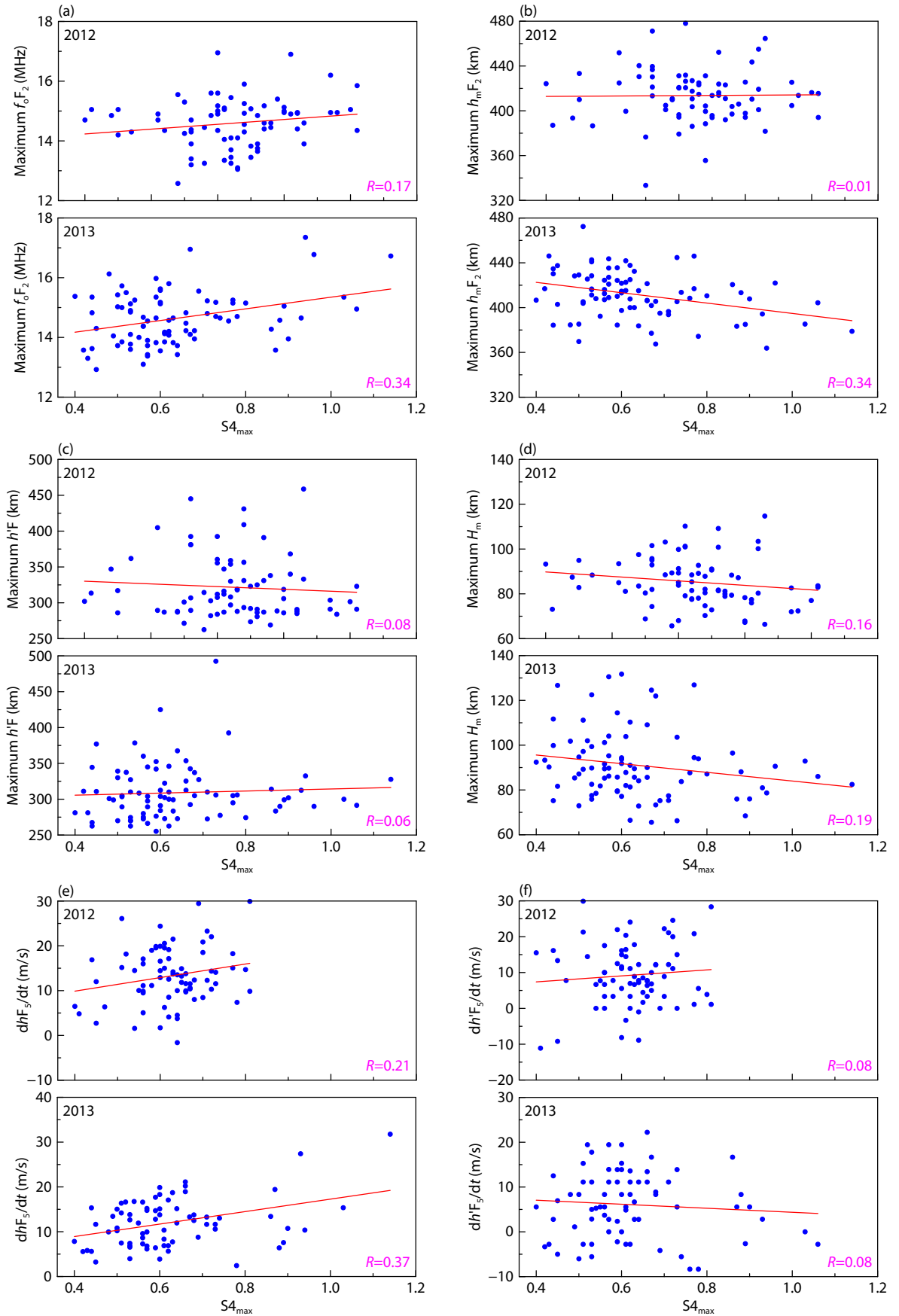


Figure 13. Correlation between the daily maximum f_oF_2 (a), h_mF_2 (b), minimum $h'F$ (c), scale height (d), the dhF_5/dt (e), dhF_5/dt (f) and the daily maximum S4 ($S4_{max}$) in equinoctial months (March–April, September–October) of 2012 and 2013.

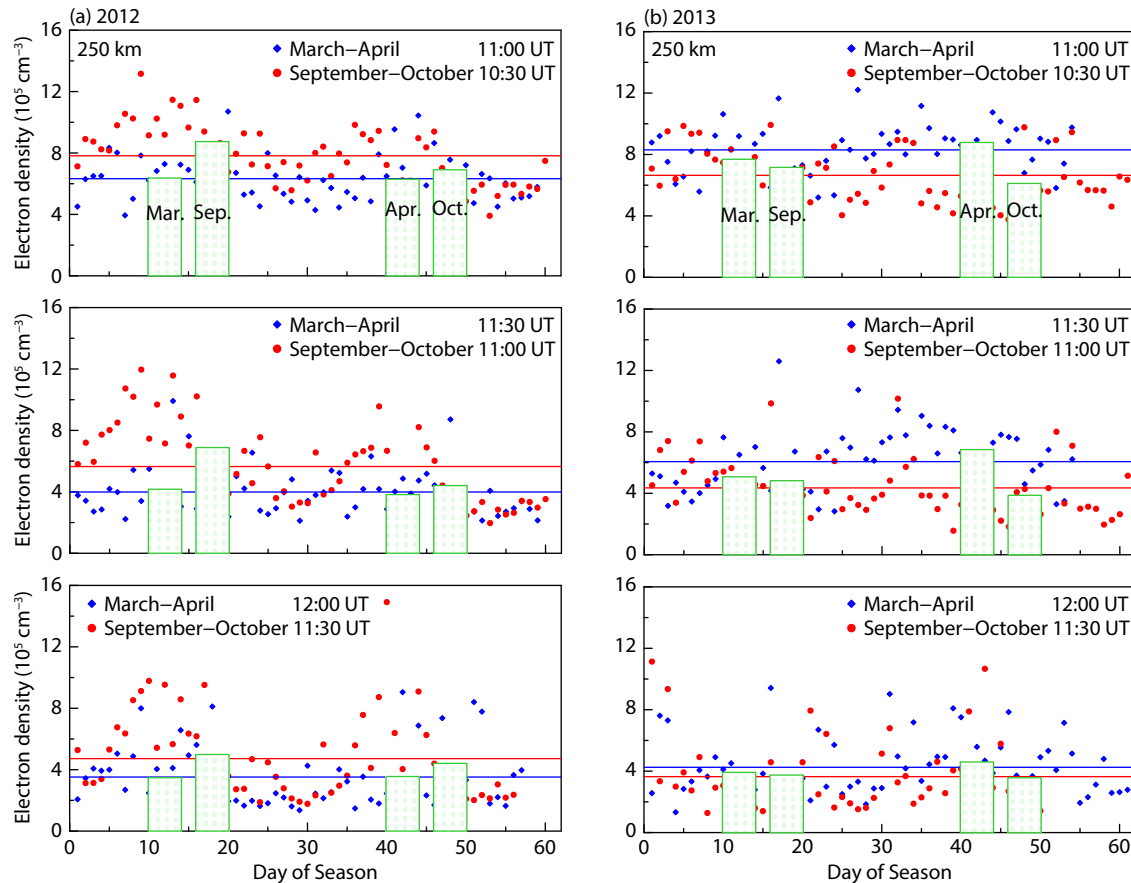


Figure 14. Day-to-day variations of the electron density at 250 km before sunset (top panel), near sunset (middle panel) and after sunset (bottom panel) from ionosonde measurements in equinoctial months of 2012 (a) and 2013 (b). The blue and red lines represent the mean values in March–April and September–October, respectively. The green bars represent the monthly mean values in March, September, April and October.

ated mainly with the occurrence of plasma irregularities. Factors and mechanisms previously reported as causing asymmetry in plasma irregularities now appear to be key to explaining the equinoctial asymmetry of scintillation. The variations of ionospheric parameters, such as f_oF_2 , H_m , $dh'F_5/dt$, and also the density gradient, as derived from ionosonde observations, are positively or negatively correlated with variations of scintillation occurrence, shown in Figures 5–7, in particular with the maximum scintillation occurrence during equinoxes and the observed equinoctial scintillation asymmetry. These annual variational similarities between ionospheric parameters (e.g. f_oF_2 , H_m) and scintillation occurrence strongly suggest that they can be causally related.

Scintillation occurrence rates observed at Sanya in high solar activity years (2012–2013) display the evident equinoctial asymmetry that has been reported in other low-latitude regions during times of low and moderate solar activity, but the factors causing the asymmetry remain poorly understood. For instance, Nishioka et al. (2008) proposed that the flux-tube integrated F-region Pedersen conductivity may lead to the observed equinoctial asymmetry while Maruyama et al. (2009) indicated, based on ionosonde observations in moderate solar activity and model calculation, that the meridional wind might play an important role because the asymmetric wind changes the density distribution in the two hemispheres, causing asymmetries in variations of background electron density and Pedersen conductivity. But Manju

et al. (Manju et al., 2012; Manju and Haridas, 2015) figured out that the neutral dynamics (not including the neutral wind) may contribute to the equinoctial asymmetry in the occurrence of ESF at equatorial and low-latitude regions. For example, they observed that the $[O/N_2]$ was higher in vernal equinox months compared to the autumnal equinox (Manju and Haridas, 2015). The neutral dynamics would also lead to variations in electron density. Thus, background electron density may be playing a vital role in providing the equinoctial asymmetry of ESF irregularities occurrence, proposed earlier by Sripathi et al. (2011) without any observational evidence.

Other investigations have proposed that the different zonal drift reversal time may cause equinoctial asymmetry in the ESF occurrences (Sripathi et al., 2016; Afolayan et al., 2019). As described above, ionospheric parameters derived from ionosonde measurements, shown in Figures 5–7, show variations that are parallel to seasonal variations of scintillation occurrence rate. This correlation, suggesting strongly that background ionosphere parameters are causally associated with occurrences of irregularity/scintillation occurrence, invited more detailed comparison between the equinoctial asymmetry of irregularities or scintillation occurrences after sunset and parallel measurements around equinoctial sunset of various ionospheric parameters, including f_oF_2 , H_m , vertical drift, and the scale length of the vertical density gradient, as presented in Figures 8–10.

In Figures 8–10, all of these ionospheric parameters — f_oF_2 , H_m , vertical drift, and L^{-1} — are seen to display equinoctial asymmetry, consistent with the report by Hu LH et al. (2020). As shown in Figure 8, around local sunset during high solar activities, when the scintillation occurrence rate was higher, f_oF_2 was larger and H_m was smaller. In 2012, the average H_m was smaller during the Fall equinox, when the scintillation occurrence rate was higher, than it was during the Spring equinox when scintillation rates were lower. In 2013, however, the pattern was reversed: it was in the Spring that the scintillation occurrence rate was higher, but again, it was then that, compared to the opposite (in this case, Fall) equinox, the average f_oF_2 was larger and H_m was smaller. In 2012 the differences in f_oF_2 and H_m between the two equinoxes were small; so was the difference in scintillation occurrence rate, confirming the striking parallels between these phenomena.

Additionally, as shown in Figure 10, when the L^{-1} was smaller, the scintillation occurrence rate was higher. Around sunset, in 2013, the L^{-1} in September–October was larger than in March–April when the scintillation rate was higher. In 2012, the average L^{-1} was smaller after sunset and the scintillation occurrence rate was higher in the Fall equinox, but the L^{-1} differences between equinoctial months were small. These observations imply that the scale length (L) of the vertical electron density gradient may also be a factor affecting the asymmetry between scintillation occurrence rates in the two equinoxes.

In summary, we find that the scintillation occurrence rate can be related to variations of f_oF_2 , H_m , and L^{-1} . In fact, f_oF_2 has been shown to be directly related to the peak density N_mF_2 , $N_mF_2 \approx (f_oF_2)^2/80.6$ (Hargreaves, 1992). And the altitudinal profile of electron density can be described by the scale height, as the Chapman function with $N_e(h) = N_mF_2 \exp[1 - \varepsilon - \exp(-\varepsilon)]$, where $\varepsilon = (h - h_mF_2)/H_m$ (Huang XQ and Reinisch, 2001). The variations of f_oF_2 and H_m represent variations of background electron density, and L^{-1} has also been found related to the background electron density, which mean that the scintillation occurrence rate is likely to be related to the background electron density.

In Figure 14, which presents the day-to-day variations of electron density at 250 km in the equinoctial months of 2012 and 2013, based on ionosonde measurements made at around local sunset time, it can be seen that the background densities in 2012 were larger around local sunset in September–October than in March–April. In 2013, the asymmetry was reversed; electron densities were obviously larger at the time of the Spring equinox than at the Fall equinox. Again, however, variations of background density around local sunset (before, near, and after sunset) during each equinox were similar to variations of the scintillation occurrence rate.

Furthermore, the drifts around local sunset also displayed the equinoctial asymmetry in both years. As can be seen in Figure 9, the average drifts at sunset in March were larger than that in September, while the average drifts in October were larger than in April. The average drifts in the Spring equinox were comparable to those observed in the Fall equinox. In both years, the drift asymmetry became more remarkable at half an hour after sunset, with the larger drifts occurring in the Spring equinox. The previously reported equinoctial asymmetry of the vertical drift around

sunset (Ren ZP et al., 2011; Madhav Haridas et al., 2015) is thus confirmed, suggesting that the drift, too, plays an important role in the occurrence of irregularities after sunset (e.g. Huang CS, 2018), as well as scintillation, as previously proposed. It is reasonable that the asymmetric drifts lead to the asymmetric occurrence of irregularities and scintillation, as Hu LH et al. (2020).

In conclusion, the equinoctial asymmetries in occurrence rate of scintillation or irregularities that are observed during times of moderate solar activity can be attributed to different variations of background electron density at the bottom of F-layer, consistent with that proposed by Sripathi et al. (2011), as well as to differences in the scintillation observed at the anomaly compared to observations at the equator (e.g. Basu and Groves, 2001). The drift may be another factor contributing to the equinoctial asymmetry of scintillation occurrence rate, a factor that has been considered crucial to the onset of ESF.

Furthermore, scintillation onset time at low latitudes also displays equinoctial asymmetry, as reported by Liu KK et al. (2015) based on observations at Sanya in 2011–2012. They found that the average onset time during the Fall equinox was earlier than that during the Spring equinox, and they attributed the onset asymmetry to the asymmetry of the sunset time. In 2012–2013, as shown in Figure 3, the onset time during Fall equinox was again earlier than that during the Spring equinox.

Besides the sunset time, there is another interesting point that should be noted. Scintillation onset can be attributed to the occurrence of plasma irregularities associated with the development of R-T instability. When the R-T instability exhibits a larger linear growth rate, the plasma irregularity may occur earlier and the scintillation onset also is earlier. From variations of the growth rate derived from ionosonde observations and ionospheric models, displayed in Figures 11–12, we can see that the growth rates around local sunset (before, near, and after) were larger in 2021 and 2013 during the Fall equinox period than in the corresponding period around the Spring equinox. Thus, earlier scintillation onset in September–October appears to be explained by more rapid growth of R-T instability during the Fall equinox, causing the irregularities to evolve more quickly and occur earlier than during the Spring equinox.

Figure 3 reveals that the difference in sunset time between the two equinoxes was about 25 minutes (e.g. Liu KK et al., 2015), and the difference was about 40 minutes in onset times of scintillation occurrence. Faster development of R-T instability in the months of September and October results in the earlier occurrence of irregularities and scintillation; slower R-T instability development correlates with later occurrence of irregularities after sunset and also later onset of scintillation; this difference may help explain why the observed differences in times of scintillation onset between the two equinoctial periods are larger than the differences between their sunset times. We suggest that the initiation and growth of R-T instability appears to be related to the onset of plasma irregularities and scintillation.

As given in Equations (1) and (2), the scale length of the vertical density gradient, L , is an important factor to determine the linear growth rate of R-T instability, which means that the scale length of

the background density gradient is correlated with the occurrence of irregularities and scintillation. [Abdu et al. \(1982\)](#) have indicated that bottomside electron density scale length near the sunset hours determines the onset of postsunset ESF. [Manju et al. \(2009\)](#) also pointed out that L plays an important role in controlling the quiet time seasonal and solar cycle variability of ESF. Recently, [Abdu et al. \(2020\)](#) figured out that the scale length of density gradient at the bottom of the F layer is a key parameter controlling the development of equatorial and low-latitude irregularities. Combining the variations of L^{-1} shown in [Figures 7–10](#), we see that the monthly average L^{-1} around local sunset correlates with previously-noted equinoctial asymmetries, primarily because it is largest in September and October. This correlation leads us to conclude that the scale length of vertical density gradient may be an important factor affecting the onset time of scintillation/irregularities and leading to the equinoctial asymmetry in onset of scintillation/irregularities.

It should be noted that scale length may be just one among multiple factors affecting the development of R-T instability and thus the equinoctial asymmetry of scintillation onset time. In order to develop a robust model capable of forecasting ESF and scintillation occurrences, it is important to determine qualitatively and then to quantify the dependence of ESF and scintillation on each ionospheric parameter.

Other factors than L^{-1} have been investigated. [Whalen \(2009\)](#) attempted to quantify the dependence of equatorial scintillation on electron density. They found that the GHz scintillation strength, represented by the S4 maximum, was a linear function of the coinciding maximum electron density of the F₂-layer (N_mF_2), which can be derived from f_oF_2 .

In this study, we examined the relationships between the variations of daily maximum ionospheric parameters and the variation of scintillation occurrence, and also correlations between the daily maximum parameters and the daily S4 maximum in high solar activity, shown in [Figure 13](#), respectively. The results show that the correlations between the daily maximum S4 and the daily maximum values of f_oF_2 , h_mF_2 , $h'F$ and H_m were poor at Sanya in equinoctial months of 2012 and 2013, as were the correlation between the $S4_{max}$ and the drifts from the ionosonde measurements, which means that in low-latitude regions it is difficult to correlate or forecast scintillation strength based on daily maximum parameters.

A possible reason is that the plasma irregularities leading to the occurrence of scintillation at low-latitude regions come from far west ([Cesaroni et al., 2021](#)), as [Saito and Maruyama \(2006\)](#) have indicated. On the other hand, the irregularities in low-latitude regions may come from the equatorial region with the evolution and motion of equatorial irregularities. Under the effects of physical factors (e.g. zonal electric field), the irregularities initiated by R-T instability in the equatorial ionosphere would be expected to evolve nonlinearly and move to low-latitude regions; hence the scintillation strength in those regions may be correlated mainly with equatorial ionospheric parameters (e.g. vertical drift).

In addition, we observe that further study of correlations between scintillation intensity (e.g. $S4_{max}$) and variability of ionospheric

parameters (e.g. $h'F$, h_mF_2 , Total Electron Content) derived from ground and space-based observations need to be made, with greater attention to day-to-day variability in the background ionosphere. For instance, [Aswathy and Manju \(2021\)](#) recently reported that the average Equatorial Ionization Anomaly crest magnitude was linearly correlated with the peak S4 index during 16:00–18:00 LT around 77°E. But [Dabas et al. \(2007\)](#) reported that the daily GHz scintillation intensity was not well correlated with the day-to-day variations of equatorial $\mathbf{E} \times \mathbf{B}$ drift during evening hours in the Indian region.

5. Conclusions

In this study, we have investigated the relationships between ionospheric parameters and the equinoctial asymmetry of low-latitude scintillation by using data derived from ionosonde observations at Sanya in high solar activity years (2012–2013) of solar cycle 24. Our principal findings are as follows:

- (1) The equinoctial asymmetry of onset time of scintillation/irregularities at low-latitude regions appears to be associated not just with local sunset time but also with the scale length (L) of the electron density gradient, which affects initiation and growth of the R-T instability at the bottomside F-layer.
- (2) Seasonal variations of critical plasma frequency, scale height around the F₂-layer peak and scale length of vertical electron density gradient can represent the seasonal variations of scintillation occurrence. The equinoctial asymmetry of scintillation, or irregularity occurrence rate, can be related to variations of background electron density and vertical drift in the F-layer near sunset time.
- (3) Scintillation strength, representing by $S4_{max}$, was found not to be well related linearly to parameters derived from the ionosonde measurements over low latitudes. Correlations were weak between scintillation strength (e.g. $S4_{max}$) and daily maximum values of f_oF_2 , h_mF_2 , $h'F$, and H_m ; moreover, the drifts over low latitudes were weak, which need to be further studied.

We have studied relationships between ionospheric parameters and the characteristics of scintillation at times of high solar activity. Future research into these relationships should focus on times of moderate and low solar activity.

Acknowledgments

This work is supported by the Fundamental Research Funds for the Central Universities, South-Central MinZu University (Grant Number: CPT22019). We acknowledge use of ionosonde and GNSS scintillation data from the Institute of Geology and Geophysics, Chinese Academy of Sciences. The scintillation and ionosonde data were provided by Beijing National Observatory of Space Environment, Institute of Geology and Geophysics, Chinese Academy of Sciences through the Data Center for Geophysics, National Earth System Science Data Sharing Infrastructure (<http://wdc.geophys.ac.cn/>). The sunspot number, $F_{10.7}$ and ap data were downloaded from the National Geophysical Data Center (ftp://ftp.ngdc.noaa.gov/STP/GEOMAGNETIC_DATA/INDICES/KP_AP/). The ROCSAT-1 data can be downloaded from the website (<https://>

cdaweb.gsfc.nasa.gov/index.html/).

References

- Abdu, M. A., de Medeiros, R. T., and Sobral, J. H. A. (1982). Equatorial spread F instability conditions as determined from ionograms. *Geophys. Res. Lett.*, 9(6), 692–695. <https://doi.org/10.1029/GL009i006p00692>
- Abdu, M. A., Iyer, K. N., de Medeiros, R. T., Batista, I. S., and Sobral, J. H. A. (2006). Thermospheric meridional wind control of equatorial spread F and evening prereversal electric field. *Geophys. Res. Lett.*, 33(7), L07106. <https://doi.org/10.1029/2005GL024835>
- Abdu, M. A., Kherani, E. A., and Sousasantos, J. (2020). Role of bottom-side density gradient in the development of equatorial plasma bubble/spread F irregularities: solar minimum and maximum conditions. *J. Geophys. Res.: Space Phys.*, 125(10), e2020JA027773. <https://doi.org/10.1029/2020JA027773>
- Adebesin, B. O., Adeniyi, J. O., Adimula, I. A., Oladipo, O. A., Olawepo, A. O., and Reinisch, B. W. (2015). Comparative analysis of nocturnal vertical plasma drift velocities inferred from ground-based ionosonde measurements of hmF₂ and h'F. *J. Atmos. Sol.-Terr. Phys.*, 122, 97–107. <https://doi.org/10.1016/j.jastp.2014.11.007>
- Afolayan, A. O., Singh, M. J., Abdullah, M., Buhari, S. M., Yokoyama, T., and Supnithi, P. (2019). Observation of seasonal asymmetry in the range spread F occurrence at different longitudes during low and moderate solar activity. *Ann. Geophys.*, 37(4), 733–745. <https://doi.org/10.5194/angeo-37-733-2019>
- Anderson, D. N., Reinisch, B., Valladare, C., Chau, J., and Veliz, O. (2004). Forecasting the occurrence of ionospheric scintillation activity in the equatorial ionosphere on a day-to-day basis. *J. Atmos. Sol.-Terr. Phys.*, 66(17), 1567–1572. <https://doi.org/10.1016/j.jastp.2004.07.010>
- Aswathy, R. P., and Manju, G. (2021). Equatorial ionization Anomaly crest magnitude and its implications on the nocturnal equatorial ionospheric plasma irregularity characteristics. *Adv. Space Res.*, 68(10), 4129–4136. <https://doi.org/10.1016/j.asr.2021.07.019>
- Bagiya, M. S., Sridharan, R., Sunda, S., Jose, L., Pant, T. K., and Choudhary, R. (2014). Critical assessment of the forecasting capability of L-band scintillation over the magnetic equatorial region-Campaign results. *J. Atmos. Sol.-Terr. Phys.*, 110–111, 15–22. <https://doi.org/10.1016/j.jastp.2014.01.012>
- Balan, N., Jayachandran, B., Balachandran Nair, R., Namboothiri, S. P., Bailey, G. J., and Rao, P. B. (1992). HF Doppler observations of vector plasma drifts in the evening F-region at the magnetic equator. *J. Atmos. Terr. Phys.*, 54(11–12), 1545–1554. [https://doi.org/10.1016/0021-9169\(92\)90162-E](https://doi.org/10.1016/0021-9169(92)90162-E)
- Basu, B. (2002). On the linear theory of equatorial plasma instability: comparison of different descriptions. *J. Geophys. Res.: Space Phys.*, 107(A8), 1199. <https://doi.org/10.1029/2001JA000317>
- Basu, S., and Groves, K. M. (2001). Specification and forecasting of outages on satellite communication and navigation systems. In P. Song, et al. (Eds.), *Space Weather, Volume 125* (pp. 423–430). American Geophysical Union. <https://doi.org/10.1029/GM125p0423>
- Billitz D., Altadill, D., Truhlik, V., Shubin, V., Galkin, I., Reinisch, B., and Huang, X. (2017). International Reference Ionosphere 2016: from ionospheric climate to real-time weather predictions. *Space Wea.*, 15(2), 418–429. <https://doi.org/10.1002/2016SW001593>
- Bittencourt, J. A., and Abdu, M. A. (1981). A theoretical comparison between apparent and real vertical ionization drift velocities in the equatorial F region. *J. Geophys. Res.: Space Phys.*, 86(A4), 2451–2454. <https://doi.org/10.1029/JA086iA04p02451>
- Cesaroni, C., Spogli, L., Franceschi, G. D., Damasceno, J. G., Grzesiak, M., Vani, B., Monico, J. F. G., Romano, V., Alfonsi L., and Cafaro, M. (2021). A measure of ionospheric irregularities: zonal velocity and its implications for L-band scintillation at low-latitudes. *Earth Planet. Phys.*, 5(5), 450–461. <https://doi.org/10.26464/epp2021042>
- Dabas, R. S., Das, R. M., Sharma, K., Garg, S. C., Devasia, C. V., Subbarao, K. S. V., Niranjana, K., and Rama Rao, P. V. S. (2007). Equatorial and low latitude spread-F irregularity characteristics over the Indian region and their prediction possibilities. *J. Atmos. Sol.-Terr. Phys.*, 69(6), 685–696. <https://doi.org/10.1016/j.jastp.2007.01.002>
- Devasia, C. V., Jyoti, N., Subbarao, K. S. V., Viswanathan, K. S., Tiwari, D., and Sridharan, R. (2002). On the plausible linkage of thermospheric meridional winds with the equatorial spread F. *J. Atmos. Sol.-Terr. Phys.*, 64(1), 1–12. [https://doi.org/10.1016/S1364-6826\(01\)00089-X](https://doi.org/10.1016/S1364-6826(01)00089-X)
- Drob, D. P., Emmert, J. T., Meriwether, J. W., Makela, J. J., Doornbos, E., Conde, M., Hernandez, G., Noto, J., Zawdie, K. A., ... Klenzing, J. H. (2015). An update to the Horizontal Wind Model (HWM): the quiet time thermosphere. *Earth Space Sci.*, 2(7), 301–319. <https://doi.org/10.1002/2014EA000089>
- Fejer, B. G., Jensen, J. W., and Su, S. Y. (2008). Quiet time equatorial F region vertical plasma drift model derived from ROCSAT-1 observations. *J. Geophys. Res.: Space Phys.*, 113(A5), A05304. <https://doi.org/10.1029/2007JA012801>
- Galkin, I. A., Khmyrov, G. M., Kozlov, A. V., Reinisch, B. W., Huang, X. Q., and Paznukhov, V. V. (2008). The ARTIST 5. *AIP Conf. Proc.*, 974(1), 150–159. <https://doi.org/10.1063/1.2885024>
- Hargreaves, J. K. (1992). *The Solar-Terrestrial Environment*. Cambridge: Cambridge University Press.
- Haridas, M. K. M., Manju, G., and Pant, T. K. (2015). On the solar activity variations of nocturnal F region vertical drifts covering two solar cycles in the Indian longitude sector. *J. Geophys. Res.: Space Phys.*, 120(2), 1445–1451. <https://doi.org/10.1002/2014JA020561>
- Hu, L. H., Zhao, X. K., Sun, W. J., Wu, Z., Zheng, J. C., Xie, H. Y., Huang, Z. G., Ning, B. Q., and Li, G. Z. (2020). Statistical characteristics and correlation of low-latitude F region bottom-type irregularity layers and plasma plumes over Sanya. *J. Geophys. Res.: Space Phys.*, 125(8), e2020JA027855. <https://doi.org/10.1029/2020JA027855>
- Huang, C. S. (2018). Effects of the postsunset vertical plasma drift on the generation of equatorial spread F. *Prog. Earth Planet. Sci.*, 5(1), 3. <https://doi.org/10.1186/s40645-017-0155-4>
- Huang, X. Q., and Reinisch, B. W. (2001). Vertical electron content from ionograms in real time. *Radio Sci.*, 36(2), 335–342. <https://doi.org/10.1029/1999RS002409>
- Jayachandran, B., Balan, N., Rao, P. B., Sastri, J. H., and Balley, G. J. (1993). HF Doppler and ionosonde observations on the onset conditions of equatorial spread F. *J. Geophys. Res.: Space Phys.*, 98(A8), 13741–13750. <https://doi.org/10.1029/93JA00302>
- Lee, C. C. (2010). Occurrence and onset conditions of postsunset equatorial spread F at Jicamarca during solar minimum and maximum. *J. Geophys. Res.: Space Phys.*, 115(A10), A10325. <https://doi.org/10.1029/2010JA015650>
- Li, G., Ning, B., Liu, L., Ren, Z., Lei, J., and Su, S. Y. (2007). The correlation of longitudinal/seasonal variations of evening equatorial pre-reversal drift and of plasma bubbles. *Ann. Geophys.*, 25(12), 2571–2578. <https://doi.org/10.5194/angeo-25-2571-2007>
- Li, G. Z., Ning, B. Q., Zhao, B. Q., Liu, L. B., Liu, J. Y., and Yumoto, K. (2008). Effects of geomagnetic storm on GPS ionospheric scintillations at Sanya. *J. Atmos. Sol.-Terr. Phys.*, 70(7), 1034–1045. <https://doi.org/10.1016/j.jastp.2008.01.003>
- Li, G. Z., Ning, B. Q., Abdu, M. A., Yue, X. N., Liu, L. B., Wan, W. X., and Hu, L. H. (2011). On the occurrence of postmidnight equatorial F region irregularities during the June solstice. *J. Geophys. Res.: Space Phys.*, 116(A4), A04318. <https://doi.org/10.1029/2010JA016056>
- Li, G. Z., Ning, B. Q., Abdu, M. A., Wan, W. X., and Hu, L. H. (2012). Precursor signatures and evolution of post-sunset equatorial spread-F observed over Sanya. *J. Geophys. Res.: Space Phys.*, 117(A8), A08321. <https://doi.org/10.1029/2012JA017820>
- Li, G. Z., Ning, B. Q., Abdu, M. A., Otsuka, Y., Yokoyama, T., Yamamoto, M., and Liu, L. B. (2013). Longitudinal characteristics of spread F backscatter plumes observed with the EAR and Sanya VHF radar in Southeast Asia. *J. Geophys. Res.: Space Phys.*, 118(10), 6544–6557. <https://doi.org/10.1002/jgra.50581>
- Li, G. Z., Ning, B. Q., Otsuka, Y., Abdu, M. A., Abadi, P., Liu, Z. Z., Spogli, L., and Wan, W. X. (2021). Challenges to equatorial plasma bubble and ionospheric scintillation short-term forecasting and future aspects in East and Southeast Asia. *Surv. Geophys.*, 42(1), 201–238. <https://doi.org/10.1007/s10712-020-09613-5>
- Liu, K. K., Li, G. Z., Ning, B. Q., Hu, L. H., and Li, H. K. (2015). Statistical characteristics of low-latitude ionospheric scintillation over China. *Adv. Space Res.*, 55(5), 1356–1365. <https://doi.org/10.1016/j.asr.2014.12.001>

- Liu, L., Wan, W., and Ning, B. (2006). A study of the ionogram derived effective scale height around the ionospheric hmF2. *Ann. Geophys.*, 24(3), 851–860. <https://doi.org/10.5194/angeo-24-851-2006>
- Luo, W. H., Xu, J. S., and Tian, M. (2012). Investigation of hemispheric asymmetry and longitudinal variation of flux-tube integrated Rayleigh-Taylor instability. *Chin. J. Geophys. (in Chinese)*, 55(4), 1078–1087. <https://doi.org/10.6038/j.issn.0001-5733.2012.04.002>
- Luo, W. H., Xu, J. S., and Zhu, Z. P. (2013). Theoretical modeling of the occurrence of equatorial and low-latitude ionospheric irregularity and scintillation. *Chin. J. Geophys. (in Chinese)*, 56(9), 2892–2905. <https://doi.org/10.6038/cjg20130903>
- Manju, G., Devasia, C. V., and Ravindran, S. (2009). The seasonal and solar cycle variations of electron density gradient scale length during magnetically disturbed days: implications for Spread F. *Earth Planet Space*, 61(7), 913–917. <https://doi.org/10.1186/BF03353202>
- Manju, G., Haridas, M. K. M., Ravindran, S., Pant, T. K., and Ram, S. T. (2012). Equinoctial asymmetry in the occurrence of equatorial spread-F over Indian longitudes during moderate to low solar activity period 2004–2007. *Indian J. Radio Space Phys.*, 41(2), 240–246.
- Manju, G., and Haridas, M. K. M. (2015). On the equinoctial asymmetry in the threshold height for the occurrence of equatorial spread F. *J. Atmos. Sol.-Terr. Phys.*, 124, 59–62. <https://doi.org/10.1016/j.jastp.2015.01.008>
- Maruyama, T., Saito, S., Kawamura, M., Nozaki, K., Krall, J., and Huba, J. D. (2009). Equinoctial asymmetry of a low-latitude ionosphere-thermosphere system and equatorial irregularities: evidence for meridional wind control. *Ann. Geophys.*, 27(5), 2027–2034. <https://doi.org/10.5194/angeo-27-2027-2009>
- Meng, X., Fang, H. X., Li, G. Z., and Weng, L. B. (2018). Statistical characteristics of locally generated ESF during equinoctial months over Sanya. *Adv. Space Res.*, 61(9), 2227–2233. <https://doi.org/10.1016/j.asr.2017.11.040>
- Nishioka, M., Saito, A., and Tsugawa, T. (2008). Occurrence characteristics of plasma bubble derived from global ground-based GPS receiver networks. *J. Geophys. Res.: Space Phys.*, 113(A5), A05301. <https://doi.org/10.1029/2007JA012605>
- Picone, J. M., Hedin, A. E., Drob, D. P., and Aikin, A. C. (2002). NRLMSISE-00 empirical model of the atmosphere: statistical comparisons and scientific issues. *J. Geophys. Res.: Space Phys.*, 107(A12), 1468. <https://doi.org/10.1029/2002JA009430>
- Ren, Z. P., Wan, W. X., Liu, L. B., Chen, Y. D., and Le, H. J. (2011). Equinoctial asymmetry of ionospheric vertical plasma drifts and its effect on F-region plasma density. *J. Geophys. Res.: Space Phys.*, 116(A2), A02308. <https://doi.org/10.1029/2010JA016081>
- Saito, S., and Maruyama, T. (2006). Ionospheric height variations observed by ionosondes along magnetic meridian and plasma bubble onsets. *Ann. Geophys.*, 24(11), 2991–2996. <https://doi.org/10.5194/angeo-24-2991-2006>
- Shinagawa, H., Jin, H., Miyoshi, Y., Fujiwara, H., Yokoyama, T., and Otsuka, Y. (2018). Daily and seasonal variations in the linear growth rate of the Rayleigh-Taylor instability in the ionosphere obtained with GAIA. *Prog. Earth Planet. Sci.*, 5(1), 16. <https://doi.org/10.1186/s40645-018-0175-8>
- Sousasantos, J., de Oliveira Moraes, A., Sobral, J. H. A., Muella, M., T. A. H., de Paula, E. R., and Paolini, R. S. (2018). Climatology of the scintillation onset over southern Brazil. *Ann. Geophys.*, 36(2), 565–576. <https://doi.org/10.5194/angeo-36-565-2018>
- Sridharan, R., Bagiya, M. S., Sunda, S., Choudhary, R., Pant, T. K., and Jose, L. (2014). First results on forecasting the spatial occurrence pattern of L-band scintillation and its temporal evolution. *J. Atmos. Sol.-Terr. Phys.*, 119, 53–62. <https://doi.org/10.1016/j.jastp.2014.06.015>
- Sripathi, S., Kakad, B., and Bhattacharyya, A. (2011). Study of equinoctial asymmetry in the Equatorial Spread F (ESF) irregularities over Indian region using multi-instrument observations in the descending phase of solar cycle 23. *J. Geophys. Res.: Space Phys.*, 116(A11), A11302. <https://doi.org/10.1029/2011JA016625>
- Sripathi, S., Singh, R., Banola, S., Sreekumar, S., Emperumal, K., and Selvaraj, C. (2016). Characteristics of the equatorial plasma drifts as obtained by using Canadian Doppler ionosonde over southern tip of India. *J. Geophys. Res.: Space Phys.*, 121(8), 8103–8120. <https://doi.org/10.1002/2016JA023088>
- Titheridge, J. E. (1988). The real height analysis of ionograms: a generalized formulation. *Radio Sci.*, 23(5), 831–849. <https://doi.org/10.1029/R5023i005p00831>
- Wang, N., Guo, L. X., Zhao, Z. W., Ding, Z. H., and Lin, L. K. (2018). Spread-F occurrences and relationships with foF2 and h'F at low- and mid-latitudes in China. *Earth, Planets Space*, 70(1), 59. <https://doi.org/10.1186/s40623-018-0821-9>
- Wang, N., Guo, L. X., Zhao, Z. W., Ding, Z. H., Xu, T., and Sun, S. J. (2019). A comparative study of ionospheric spread-F and scintillation at low- and mid-latitudes in China during the 24th solar cycle. *Adv. Space Res.*, 63(2), 986–998. <https://doi.org/10.1016/j.asr.2018.10.010>
- Whalen, J. A. (2009). The linear dependence of GHz scintillation on electron density observed in the equatorial anomaly. *Ann. Geophys.*, 27(4), 1755–1761. <https://doi.org/10.5194/angeo-27-1755-2009>
- Wu, Q. (2015). Longitudinal and seasonal variation of the equatorial flux tube integrated Rayleigh-Taylor instability growth rate. *J. Geophys. Res.: Space Phys.*, 120(9), 7952–7957. <https://doi.org/10.1002/2015JA021553>
- Wu, Q. (2017). Solar effect on the Rayleigh-Taylor instability growth rate as simulated by the NCAR TIEGCM. *J. Atmos. Sol.-Terr. Phys.*, 156, 97–102. <https://doi.org/10.1016/j.jastp.2017.03.007>
- Xu, T., Wu, Z. S., Hu, Y. L., Wu, J., Suo, Y. C., and Feng, J. (2010). Statistical analysis and model of spread F occurrence in China. *Sci. China Technol. Sci.*, 53(6), 1725–1731. <https://doi.org/10.1007/s11431-010-3169-3>
- Yue, X. N., Wan, W. X., Lei, J. H., and Liu, L. B. (2008). Modeling the relationship between ExB vertical drift and the time rate of change of hmF2 ($\Delta\text{hmF2}/\Delta t$) over the magnetic equator. *Geophys. Res. Lett.*, 35(5), L05104. <https://doi.org/10.1029/2007GL033051>
- Zhang, Y., Wan, W., Li, G., Liu, L., Hu, L., and Ning, B. (2015). A comparative study of GPS ionospheric scintillations and ionogram spread F over Sanya. *Ann. Geophys.*, 33(11), 1421–1430. <https://doi.org/10.5194/angeo-33-1421-2015>